ADVANCED FUNCTIONAL MATERIALS
www.afm-journal.de

Check for updates

Effects of Elemental Modulation on Phase Purity and Electrochemical Properties of Co-free High-Entropy Spinel Oxide Anodes for Lithium-Ion Batteries

Jagabandhu Patra, Thi Xuyen Nguyen, Chia-Chien Tsai, Oliver Clemens, Ju Li, Pratibha Pal, Weng Kent Chan, Chih-Heng Lee, Hsin-Yi Tiffany Chen, Jyh-Ming Ting, and Jeng-Kuei Chang**

High entropy oxide (HEO) is a new class of lithium-ion battery anode with high specific capacity and excellent cyclability. The beauty of HEO lies in the unique tailorable properties with respect to tunable chemical composition, which enables the use of infinite element combinations to develop new electrode materials. This study synthesizes a series of Co-free spinel-type HEOs via a facile hydrothermal method. Based on quaternary medium-entropy $(CrNiMnFe)_3O_4$, the fifth elements of V, Mg, and Cu are added, and their ability to form single-phase HEOs is investigated. It is demonstrated that the chemical composition of HEOs is critical to the phase purity and corresponding charge–discharge performance. The oxygen vacancy concentration seems to be decisive for the rate capability and reversibility of the HEO electrodes. An inactive spectator element is not necessary for achieving high cyclability, given that the phase purity of the HEO is wisely controlled. The single-phase $(CrNiMnFeCu)_3O_4$ shows a great high-rate capacity of 480 mAh g^{-1} at 2000 mA g^{-1} and almost no capacity decay after 400 cycles. Its phase transition behavior during the lithiation/delithiation process is characterized with operando X-ray diffraction. A $(CrNiMnFeCu)_3O_4||LiNi_{0.8}Co_{0.1}Mn_{0.1}O_2$ cell is constructed with 590 Wh kg^{-1} (based on electrode materials) gravimetric energy density.

1. Introduction

Li-ion batteries (LIBs) are the dominant energy storage devices for portable electronics, electric vehicles, and grid electricity management due to their high energy density, long cycle life, and great cost-effectiveness.[1] The Nobel prize was awarded in 2019 to the three pioneer LIB researchers.[2] Increasing the energy density is always an imperative topic for the advancement of LIBs. The traditional anode material of graphite is limited by its relatively low specific capacity of ≈350 mAh g^{-1}, sluggish Li^+ transport, and potential Li metal deposition.[3,4] The development of alternative anode materials with better Li^+ storage capacities and reaction kinetics is in high demand.

Transitional metal oxides (TMOs) have been explored as conversion-type anodes for the next-generation LIBs.[5] The conversion reactions enable the multi-electron transfer, thereby providing large specific capacities (>1000 mAh g^{-1}).[6,7] With a

J. Patra, J.-K. Chang
Department of Materials Science and Engineering
National Yang Ming Chiao Tung University
1001 University Road, Hsinchu 30010, Taiwan
E-mail: jkchang@nctu.edu.tw

J. Patra, J.-M. Ting, J.-K. Chang
Hierarchical Green-Energy Materials (Hi-GEM) Research Center
National Cheng Kung University
1 University Road, Tainan 70101, Taiwan
E-mail: jting@mail.ncku.edu.tw

T. X. Nguyen, C.-C. Tsai, P. Pal, J.-M. Ting
Department of Materials Science and Engineering
National Cheng Kung University
1 University Road, Tainan 70101, Taiwan

O. Clemens
Universität Stuttgart
Institut für Materialwissenschaft
Chemische Materialsynthese
Heisenbergstraße 3, 70569 Stuttgart, Germany

J. Li
Department of Nuclear Science and Engineering
and Department of Materials Science and Engineering
Massachusetts Institute of Technology
77 Massachusetts Avenue, Cambridge, MA 02139, USA

W. K. Chan, C.-H. Lee, H.-Y. T. Chen
Department of Engineering and Systems Science
National Tsing Hua University
Hsinchu 300044, Taiwan

The ORCID identification number(s) for the author(s) of this article can be found under https://doi.org/10.1002/adfm.202110992.

DOI: 10.1002/adfm.202110992

 © 2022 Wiley-VCH GmbH

16163028, 2022, 17, Downloaded from https://onlinelibrary.wiley.com/doi/10.1002/adfm.202110992 by Massachusetts Institute of Technolo, Wiley Online Library on [31/07/2023]. See the Terms and Conditions (https://onlinelibrary.wiley.com/terms-and-conditions) on Wiley Online Library for rules of use; OA articles are governed by the applicable Creative Commons License

relatively high redox potential, this type of anode has less risk of forming metallic Li during battery charging. However, traditional TMOs suffer from severe structural degradation, which is associated with crystallinity and volume change during lithiation/delithiation, and low electronic/ionic conductivity. The volume expansion can exceed 150% as reported in the literature.[8–10] These result in inferior electrode cycling stability and rate capability.[8,11] Recently, the emergence of a new class of high entropy oxide (HEO) materials has attracted attention for developing advanced LIBs.[12–14] The key concept of HEO is to use multiple constituents (usually five or more components with each concentration being 5–35%) to increase the configurational entropy (i.e., $S_{\text{config.}} \geq 1.5\ R$), which is a phase-stabilization driving force.[12–14] Entropy stabilized HEOs were first reported by Rost et al. in 2015.[15] Since then, HEOs have been applied across various fields, including energy storage, catalysis, and dielectric/magnetic/optical applications.[16–21] The HEO lattice is distorted due to the different sizes of accommodated atoms, causing a lattice residual stress that can alter material properties.[22] Thus, the HEOs exhibit tailorable physicochemical properties depending on the constituent elements.

Sarkar et al. developed rock-salt (CoCuMgNiZn)O as an LIB anode that can deliver good stability over 500 cycles owing to the entropy stabilization effects.[23] They also showed that the entropy change due to various elemental combinations led to distinct charge–discharge behavior. Qiu et al. compared the performance of Co_3O_4 with (CoCuMgNiZn)O HEO.[24] They proposed that an appropriate amount of inactive MgO formed after lithiation could buffer the volume change and restrain aggregation of the active nanograins, improving the cycling and rate performance of the HEO electrode. Ghigna et al. studied the lithiation/delithiation mechanism of the $Mg_{0.2}Co_{0.2}Ni_{0.2}Cu_{0.2}Zn_{0.2}O$ anode using operando X-ray absorption spectroscopy.[25] Besides the rock-salt-structure HEOs above, spinel-type HEOs (HESOs) are interesting because of their two Wyckoff sites and plenty of oxygen vacancies, which are favorable for reversible Li^+ storage.[26] A nonequimolar $(CrMnFeCoNi)_3O_4$ HESO synthesized via a surfactant-assisted hydrothermal method was reported to have a high specific capacity and long cycle life.[26] We have used combined scanning transmission electron microscopy and electron energy-loss spectroscopy technique to study the crystal structure and valence state evolution of the HESO electrode at various charge–discharge potentials.[27] Chen et al. performed operando synchrotron X-ray spectroscopy and microscopy studies on the synthesized $(NiCoMnFeTi)_3O_4$ anode.[28] The rock-salt and spinel HEO anodes have shown a great potential for LIB applications. However, further fundamental investigation on the material property–electrochemical behavior correlation is much needed.

Most of the reported HEO anodes consist of Co, which provides high conductivity and has great compatibility with other constituent elements.[29] It was reported that, without Co, the HEO electrode showed a significant capacity decay after approximately ten cycles.[23] However, Co is scarce, toxic, expensive, and usually suffers from geopolitical interference and a vulnerable global supply problem. Thus, Co-based HEOs are not good candidates for large-scale applications.[30] Developing Co-free earth-abundant electrode materials is highly desirable. Actually, the chemical composition plays a critical role in determining the electrochemical performance of HEO electrodes.[31–33] Various constituent elements can give rise to different redox potentials, charge–discharge capacities, and reversibility. Moreover, the solid-solution single-phase formation ability of the compositional elements is also of great concern. An earlier report suggested that, without Mg^{2+} or Ni^{2+}, single-phase HEO cannot be formed even at high temperatures,[23] which indicated a phase stabilization function of these cations. Understanding the effects of the chemical composition of HEOs on their phase purity and the corresponding lithiation/delithiation properties is critical, but has not been investigated. This topic is addressed in this work.

In the present study, we develop a series of Co-free HESO anodes via a facile hydrothermal method. We start with a quaternary $(CrNiMnFe)_3O_4$ (denoted as 4M) because these elements, neighboring to Co in the periodic table, are relatively low-cost, earth-abundant, and environmentally friendly. They have similar ionic radii and exhibit good chemical compatibility. Then, the material composition is modulated with the addition of V, Mg, and Cu to form $(CrNiMnFeV)_3O_4$(4MV), $(CrNiMnFeMg)_3O_4$(4MMg), and $(CrNiMnFeCu)_3O_4$(4MCu) HESOs, respectively. The high valence of V (next to Cr in the periodic table) could increase the electrode capacity, Mg is known to act as a structural pillar,[24,25] and Cu is inexpensive and close to Ni in the size. Therefore, these three elements are selected. The morphology, crystallinity, microstructures, valence states, and electrochemical charge–discharge properties of the HESOs are systematically studied. In addition, the lithiation/delithiation behavior is examined using operando X-ray diffraction (XRD). A 4MCu‖$LiNi_{0.8}Co_{0.1}Mn_{0.1}O_2$ full cell is constructed to evaluate the practical feasibility of the HESO anode. For the first time, we demonstrate that various elemental compositions of HESOs give rise to different impurity phase fractions, which significantly affects the electrochemical performance of the HESO anodes.

2. Results and Discussion

The morphologies of the as-synthesized 4M, 4MV, 4MMg, and 4MCu samples were characterized using scanning electron microscopy (SEM), and the micrographs are shown in **Figure 1**a–d. The 4M sample consists of irregular particles with non-uniform sizes ranging from 100 nm to nearly 1 μm. For 4MV, two distinct morphologies were observed, namely nanoparticles (≈100 nm) and micro-sized chunks. The 4MMg shows nanoparticles having uniform sizes (<100 nm). The 4MCu is composed of connecting particles having diameters of ≈200–300 nm. The crystal structures of the samples were investigated using XRD. The obtained patterns, together with the Rietveld fitting results, are shown in Figure 1e–h. For the 4M sample, asymmetric diffraction peaks were observed, which consisted of two spinel structures with different lattice parameters. A small fraction of bixbyite-structure (*Ia-3*) Mn_2O_3 was also found in this sample. For 4MV and 4MMg, besides the major spinel structure (*Fd-3m*), impurity phases of $Mn_2V_2O_7$ (*C12/m1*) and rock-salt oxide (*Fm-3m*) were found, respectively. Only the 4MCu sample exhibited a single-phase spinel structure. The details of phase

 © 2022 Wiley-VCH GmbH

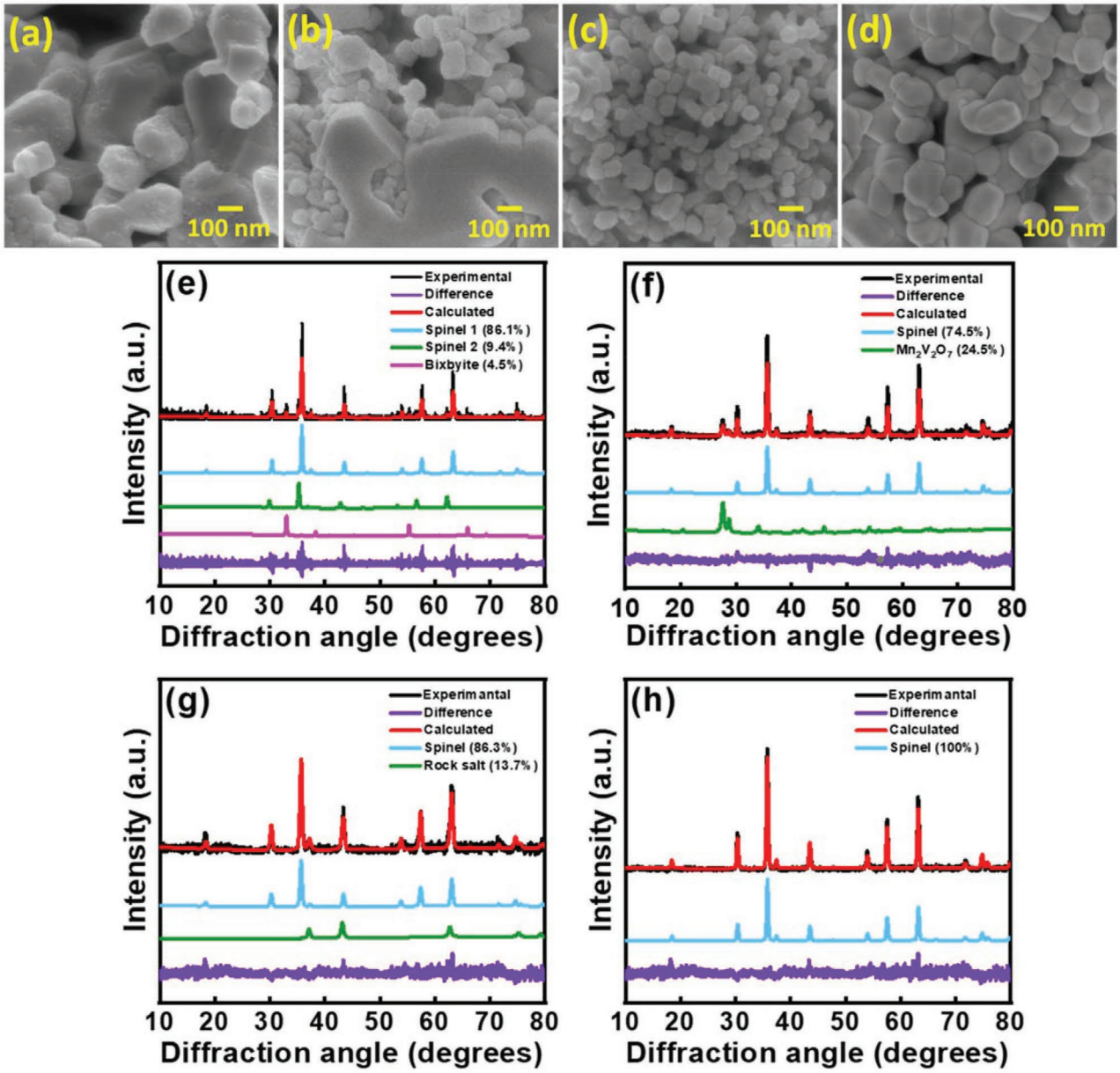

Figure 1. SEM images of as-synthesized a) 4M, b) 4MV, c) 4MMg, and d) 4MCu samples. XRD patterns and corresponding Rietveld fittings of e) 4M, f) 4MV, g) 4MMg, and h) 4MCu samples.

compositions and Rietveld refinement results of these samples are shown in Tables S1–S4 (Supporting Information).

Transmission electron microscopy (TEM) analyses were further conducted on the 4M and 4MCu, as shown in Figure S1 (Supporting Information) and **Figure 2**, respectively. A lattice fringe having a 0.30 nm spacing, which belongs to the (220) plane distance of the spinel structure, is seen in the high-resolution TEM image (Figure 2b). The *d* spacings calculated from the selected area electron diffraction (SAED) pattern in Figure 2c are well consistent with the XRD data. A high-angle annular dark-field (HAADF) image and energy-dispersive X-ray spectroscopy (EDS) elemental mapping data are given in Figure 2d. Homogeneous distribution of all the elements was found. Figure S1 (Supporting Information) shows the TEM analysis results of the 4M sample. In the high-resolution lattice image, both spinel (*Fd-3m*) and bixbyite (*Ia-3*) structures are seen, with the corresponding fast Fourier transform images shown in Figure S1d,f (Supporting Information), respectively.

Table S5 (Supporting Information) shows the inductively coupled plasma-mass spectroscopy (ICP-MS) data and the calculated configurational entropy values of the samples. Basically, all the constituent elements have similar concentrations. The entropy value of the 4M sample is 1.383 *R*, which is considered as a medium-entropy oxide. The values for the 4MV, 4MMg, and 4MCu are 1.608 *R*, 1.608 *R*, and 1.600 *R*, respectively, indicating that all of them are HESOs. X-ray photoelectron

© 2022 Wiley-VCH GmbH

16163028, 2022, 17, Downloaded from https://onlinelibrary.wiley.com/doi/10.1002/adfm.202110992 by Massachusetts Institute of Technolo, Wiley Online Library on [31/07/2023]. See the Terms and Conditions (https://onlinelibrary.wiley.com/terms-and-conditions) on Wiley Online Library for rules of use; OA articles are governed by the applicable Creative Commons License

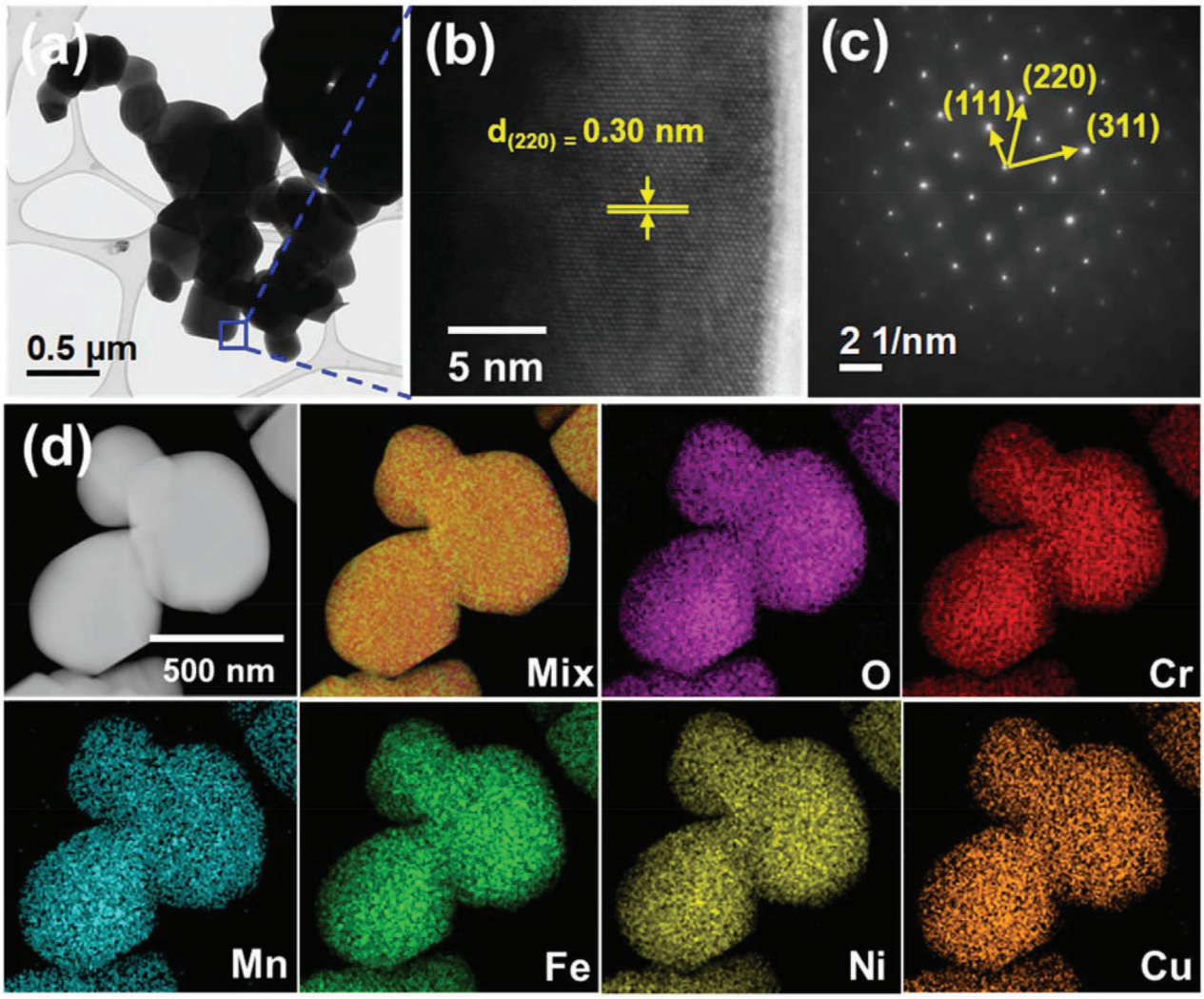

Figure 2. a) TEM image, b) high-resolution lattice image, c) SAED pattern, and d) HAADF image/EDS mapping data of as-synthesized 4MCu sample.

spectroscopy (XPS) analyses were performed to investigate the valence states of the constituent elements, as shown in **Figure 3**. The data indicate that the Mn, Fe, Ni cations in 4M, 4MV, 4MMg, and 4MCu exhibit mixed divalent/trivalent states, while the Cr cation is mainly in the Cr^{3+} state with a small portion of Cr^{6+}. In the Cr 2p spectra (Figure 3a), the peaks at 576.0 eV (Cr $2p_{3/2}$) and 578.1 eV (Cr $2p_{3/2}$) are assigned to Cr^{3+} and Cr^{6+}, respectively.[34] The Cr^{3+}/Cr^{6+} ratios are 72:28, 76:24, 78:22, and 78:22 for 4M, 4MV, 4MMg, and 4MCu, respectively. The Cr $2p_{1/2}$ peak is located at 586.2 eV.[35] In the Mn $2p_{3/2}$ spectra (Figure 3b), the peak at 641.2 eV belongs to Mn^{2+}, while the peak at 643.2 eV is attributed to Mn^{3+}.[36] The Mn^{2+}/Mn^{3+} ratios of 4M, 4MV, 4MMg, and 4MCu are 76:24, 72:28, 70:30, and 63:37, respectively. A satellite peak was observed at 646.2 eV. Two peaks at 709.9 and 712.2 eV in the Fe $2p_{3/2}$ spectra (Figure 3c) are attributed to the Fe^{2+} and Fe^{3+}, respectively.[37] In addition, two peaks located at 714.6 and 718.5 eV are the Fe^{2+} and Fe^{3+} satellite peaks.[38] The calculated Fe^{2+}/Fe^{3+} ratios are 52:48, 61:39, 61:39, and 63:37 for 4M, 4MV, 4MMg, and 4MCu, respectively. In the Ni 2p XPS spectra (Figure 3d), the peaks at 854.6 and 856.2 eV are assigned to the Ni^{2+} and Ni^{3+} oxidation states, respectively.[39] The Ni^{2+}/Ni^{3+} ratios of 4M, 4MV, 4MMg, and 4MCu are 66:33, 65:35, 68:32, and 67:33, respectively. The 872.7 eV peak is attributed to the Ni $2p_{1/2}$.[40] The peaks at 861.3 and 879.8 eV are shake-up satellites of Ni $2p_{3/2}$ and Ni $2p_{1/2}$, respectively.[41] The XPS spectra of V $2p_{3/2}$, Mg 1s, and Cu 2p for the 4MV, 4MMg, and 4MCu samples, respectively, are shown in Figure 3e–g. Two valence states of V^{5+} and V^{4+} are found with a V^{4+}/V^{5+} ratio of 17/83, whereas the Mg is in the divalent state. The Cu spectrum shows the co-existence of Cu^{+} and Cu^{2+} (with a Cu^{+}/Cu^{2+} ratio of 25/75). From the ICP-MS and XPS data, the average cation oxidation states of 4M, 4MV, 4MMg, and 4MCu are calculated to be 2.74, 3.21, 2.55, and 2.58, respectively. The clearly higher valence state of 4MV is associated with a high fraction of $Mn_2V_2O_7$ impurity phase, in which V^{5+} is present. The O 1s spectra (Figure 3h) can be deconvoluted into three components at 529.6 eV, 530.8 eV, and 532.5 eV, which correspond to lattice oxygen (O_L), defective oxygen (related to oxygen vacancies; O_V), and surface chemically absorbed oxygen (O_C), respectively.[42,43] The O_V content of the 4MCu is 26.8%,

© 2022 Wiley-VCH GmbH

16163028, 2022, 17, Downloaded from https://onlinelibrary.wiley.com/doi/10.1002/adfm.202110992 by Massachusetts Institute of Technolo, Wiley Online Library on [31/07/2023]. See the Terms and Conditions (https://onlinelibrary.wiley.com/terms-and-conditions) on Wiley Online Library for rules of use; OA articles are governed by the applicable Creative Commons License

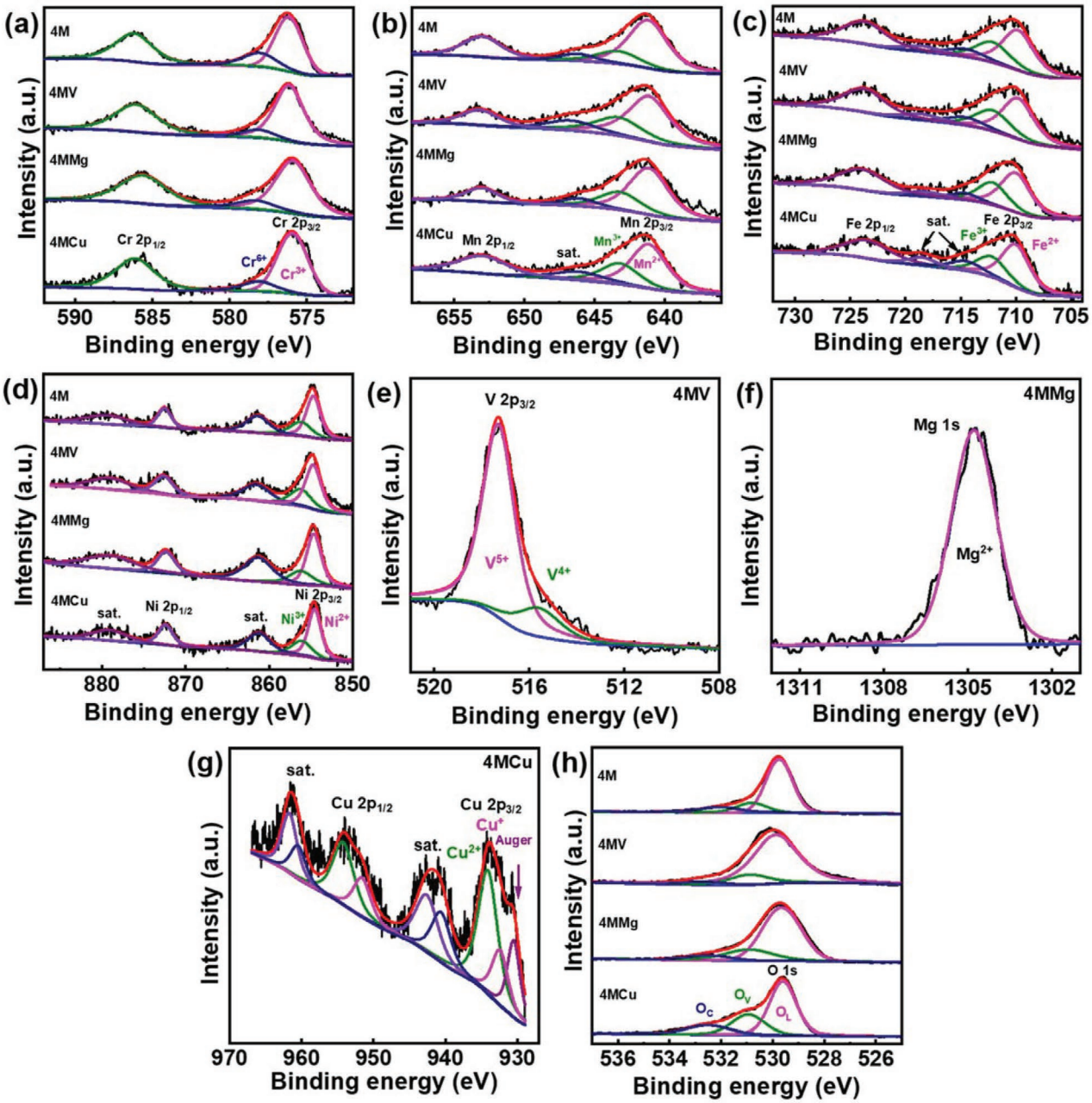

Figure 3. High-resolution XPS a) Cr 2p, b) Mn 2p, c) Fe 2p, d) Ni 2p, e) V $2p_{3/2}$, f) Mg 1s, g) Cu 2p, and h) O 1s spectra of various samples.

followed by 21.7% of 4MMg, 16.7% of 4MV, and 15.5% of 4M. Clearly, the O_V concentration of the 4M sample is lower than those of the other HESOs. The highest O_V ratio of 4MCu is consistent with the electron paramagnetic resonance data shown in Figure S2 (Supporting Information), where a higher signal intensity means a higher O_V concentration.

Cyclic voltammetry (CV) tests were performed to study the electrochemical characteristics of the 4M, 4MV, 4MMg, and 4MCu electrodes. Figure S3 (Supporting Information) shows the initial five CV cycles with a series of redox peaks. During the first negative scan, multiple cathodic peaks were observed, which can be attributed to electrolyte decomposition (thus solid electrolyte interphase (SEI) formation), stepwise reduction reactions of the electrodes, and Li_2O evolution.[32,25] For 4MV and 4MCu, the major conversion reaction peaks are located at ≈0.3 V, which are clearly shifted negatively for 4M and 4MMg. This indicates that the former two electrodes have higher electroactivity for uptake of Li^+. In the following positive scan, the anodic current before 1.2 V was steady and a broad oxidation peak was found at ≈1.5 V, indicating that a re-conversion (i.e., Li^+ release) reaction took place.[33,44] In the second cycle, the cathodic peaks of all electrodes moved toward lower overpotential, reflecting that the lithiation processes became facilitated. It is noted that both the reduction and oxidation curves basically overlapped from the second cycle

© 2022 Wiley-VCH GmbH

16163028, 2022, 17, Downloaded from https://onlinelibrary.wiley.com/doi/10.1002/adfm.202110992 by Massachusetts Institute of Technolo, Wiley Online Library on [31/07/2023]. See the Terms and Conditions (https://onlinelibrary.wiley.com/terms-and-conditions) on Wiley Online Library for rules of use; OA articles are governed by the applicable Creative Commons License

onward. Great redox reversibility of the electrodes was achieved. Figure S3c (Supporting Information) also reveals that the 4MMg electrode showed a relatively small CV current, which implies an inferior charge storage capability of this electrode.

To evaluate the Li^+ storage properties of the oxide electrodes, galvanostatic charge–discharge tests were performed. Figure S4 (Supporting Information) shows the initial charge–discharge curves of the electrodes measured at 50 mA g^{-1}. As revealed, the first lithiation curves show clear voltage plateaus below 0.5 V, which are consistent with the CV data. The first-cycle Coulombic efficiency (CE) loss is ascribed to the SEI formation and irreversible trap of Li^+ within the electrode. The initial CE (defined as delithiation capacity/lithiation capacity × 100%) values of 4M, 4MV, 4MMg, and 4MCu electrodes are 64%, 63%, 61%, and 70%, respectively. The relatively lower CE of the 4MMg electrode can be attributed to its smaller particle size (Figure 1c), which inevitably increases the interfacial area with liquid electrolyte and thus leads to excessive SEI formation. In contrast, the high-phase-purity 4MCu HESO electrode showed a superior CE value. We believe that this is associated with the high-entropy effects that stabilize the oxide crystal structure and thus enhance the lithiation/delithiation reversibility.[16,23,45] As shown in Figure S4 (Supporting Information), the charge–discharge properties of all electrodes became stable after the first cycles, with the CE values being ≈99%.

Figure 4a–d shows the charge–discharge curves of the oxide electrodes. With progressively increasing the current rate from 50 to 2000 mA g^{-1}, the specific capacities gradually decreased due to the kinetic limitation during the lithiation/delithiation processes.[46,47] At 50 mA g^{-1}, the reversible capacities of the 4M, 4MV, 4MMg, and 4MCu electrodes are 750, 1005, 590, and 800 mA h g^{-1}, respectively. The 4MV offered the highest specific capacity owing to the high valence state of V that could provide a wide range of valence changes during charging/discharging. For 4MMg, because the Mg component is electrochemically inactive,[24] a relatively low capacity was measured. However,

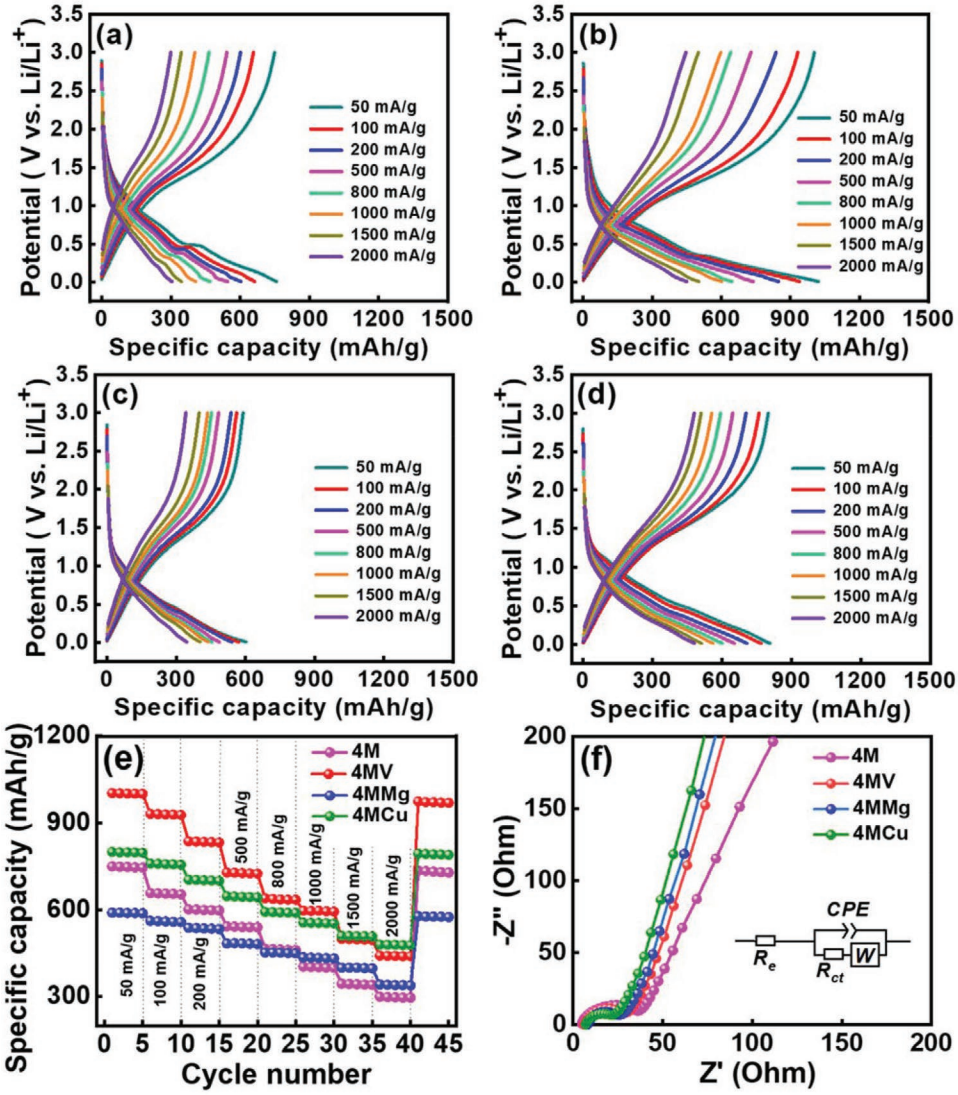

Figure 4. Charge–discharge curves of a) 4M, b) 4MV, c) 4MMg, and d) 4MCu electrodes were measured at various rates. e) Comparative rate capability of various electrodes. f) EIS Nyquist spectra of various electrodes after three conditioning cycles.

© 2022 Wiley-VCH GmbH

16163028, 2022, 17, Downloaded from https://onlinelibrary.wiley.com/doi/10.1002/adfm.202110992 by Massachusetts Institute of Technolo, Wiley Online Library on [31/07/2023]. See the Terms and Conditions (https://onlinelibrary.wiley.com/terms-and-conditions) on Wiley Online Library for rules of use; OA articles are governed by the applicable Creative Commons License

16163028, 2022, 17, Downloaded from https://onlinelibrary.wiley.com/doi/10.1002/adfm.202110992 by Massachusetts Institute of Technolo, Wiley Online Library on [31/07/2023]. See the Terms and Conditions (https://onlinelibrary.wiley.com/terms-and-conditions) on Wiley Online Library for rules of use; OA articles are governed by the applicable Creative Commons License

the obtained capacities of all the HESOs are considerably higher than that (≈350 mAh g^{-1}) of the conventional graphite anode. Figure 4e and Table S6 (Supporting Information) compare the rate capability of various electrodes. At a high specific current of 2000 mA g^{-1}, the 4M, 4MV, 4MMg, and 4MCu electrodes showed reversible capacities of 300, 442, 342, and 480 mAh g^{-1}, respectively, corresponding to 40%, 44%, 58%, and 60% capacity retention compared to the values measured at 50 mA g^{-1}. When the current rate decreased back to 50 mA g^{-1}, the capacities were restored, as shown in Figure 4e. Although the 4M electrode, similar to traditional TMO electrodes,[48–51] exhibited unsatisfactory kinetics at high rates, the other HESO electrodes demonstrated clearly improved rate capability. Compared to 4MV, the 4MMg showed superior rate performance due to its smaller particle size, which can reduce Li^+ diffusion distances and increase the electrode–electrolyte interface area. However, the pure-phase 4MCu, even having a larger particle size than that of 4MMg, showed the best high-rate property. Clearly, there is another factor (that will be discussed later) that also determines the electrode kinetics.

Generally, conventional TMO anodes suffer from a significant capacity decay at a high charge–discharge rate. For example, ZnO/C delivered 180 mAh g^{-1}@1000 mA g^{-1}, CuO/CNT delivered ≈275 mAh g^{-1}@1340 mA g^{-1}, Cu_2S/C delivered ≈250 mAh g^{-1}@1685 mA g^{-1}, $Ni_xCo_{3-x}O_4$ nanosheets delivered 293 mAh g^{-1}@1600 mA g^{-1}, Fe_2O_3/graphene delivered ≈425 mAh g^{-1}@2000 mA g^{-1}, $Mn_xCo_{1-x}Fe_2O_4$ delivered 115 mAh g^{-1}@2000 mA g^{-1}.[48–53] Our 4MCu also outperforms many recently reported HEOs in terms of high-rate performance, such as $(Co_{0.2}Cu_{0.2}Mg_{0.2}Ni_{0.2}Zn_{0.2})O$ (≈280 mAh g^{-1}@1000 mA g^{-1}), $(Ni_{0.2}Co_{0.2}Mn_{0.2}Fe_{0.2}Ti_{0.2})O$ (401 mAh g^{-1}@1000 mA g^{-1}), $(Mg_{0.2}Ti_{0.2}Zn_{0.2}Cu_{0.2}Fe_{0.2})_3O_4$ (272 mAh g^{-1}@2000 mA g^{-1}), $(FeNiCrMnZn)_3O_4$ (≈300 mAh g^{-1}@2000 mA g^{-1}), $(FeCoNiCrMn)_3O_4$ (≈180 mAh g^{-1}@2000 mA g^{-1}), $(FeCoNiCrMnZnLi)_3O_4$ (≈173 mAh g^{-1}@2000 mA g^{-1}), and $(Mg_{0.2}Co_{0.2}Ni_{0.2}Cu_{0.2}Zn_{0.2})O$ (≈300 mAh g^{-1}@1800 mA g^{-1}).[23,28,32,33,54,55] The fast charging–discharging characteristics of the proposed 4MCu HESO electrode is promising.

Figure 4f shows the electrochemical impedance spectroscopy (EIS) spectra of the 4M, 4MV, 4MMg, and 4MCu electrodes after three conditioning cycles. The figure inset shows the equivalent circuit to characterize these spectra. The R_e represents the ohmic resistance (which is dominated by electrolyte resistance),[56,57] R_{ct} represents the charge-transfer resistance, *CPE* is the interfacial constant phase element, and *W* is the Warburg impedance associated with Li^+ transport.[58] The fitting results show that the R_{ct} values for the 4M, 4MV, 4MMg, and 4MCu electrodes are 37, 30, 25, and 20 Ω, respectively. The Li^+ diffusion coefficient (D_{Li}^+) can be estimated from the EIS sloping line at low frequency.[59] As shown in **Table 1**, the 4MCu has the highest D_{Li}^+ value of 6.5×10^{-12} cm^2 s^{-1} among the electrodes. This is ascribed to the high O_v concentration of 4MCu (Figure 3h), which can modulate the electronic structure and promotes Li^+ transport.[60,61] The R_{ct} and D_{Li}^+ values are in line with the high-rate performance of the oxide electrodes.

Table 1. R_{ct} and D_{Li}^+ values of various electrodes before and after 400 charge–discharge cycles.

	Before cycling		After 400 cycles	
	R_{ct} (Ω)	D_{Li}^+ (cm^2 s^{-1})	R_{ct} (Ω)	D_{Li}^+ (cm^2 s^{-1})
4M	37	5.4×10^{-13}	80	1.3×10^{-15}
4MV	30	1.5×10^{-12}	60	8.2×10^{-15}
4MMg	25	4.3×10^{-12}	48	6.6×10^{-14}
4MCu	20	6.5×10^{-12}	22	4.4×10^{-13}

To examine the phase transition behavior of the 4MCu electrode during electrochemical lithiation/delithiation, in operando XRD analysis was performed. The obtained diffraction patterns of two charge–discharge cycles are shown in **Figure 5**. The spinel (M_3O_4) diffraction peaks gradually diminished during the first lithiation. At ≈0.35 V, the peaks at ≈37° and ≈43° emerged, indicating the formation of a rock-salt-type mono-oxide (MO). Both M_3O_4 and MO peaks became faint upon further lithiation (below ≈0.2 V). This suggests that the long-range lattice ordering was broken, leaving only short-range ordering in the structure,[23,24,27] which was hardly detectable via XRD. Above phase, the transformation could involve trapping of Li^+ ions and lattice stress within the HESO,[28] leading to the first-cycle efficiency loss. In the following delithiation process, no clear peak emerged. During the second-cycle charge and discharge, the nano-crystalline nature of the HESO was still preserved. The nano-crystals have less rigid lattices,[28,62] which may allow more freedom for rearrangement of the electrode atoms during lithiation/delithiation, leading to great electrochemical reversibility.

Figure 6a shows the cycling stability of the electrodes (after three conditioning cycles) evaluated at a rate of 500 mA g^{-1}. After 400 cycles, the 4M, 4MV, 4MMg, and 4MCu electrodes retained 2%, 10%, 95%, and 100% of the initial capacities, respectively. Figure 6b–e shows the corresponding postmortem SEM images. The capacity fluctuation, which was also observed for other HEO electrodes in the literature,[23,24,26,55] could be associated with the chemical composition and structural variation of the electrodes during cycling.[23,55] The exact mechanism requires further investigation. The average CE values for 4M and 4MV are ≈99%, whereas the values for 4MMg and 4MCu are above 99.5%. The medium-entropy 4M electrode exhibited significant capacity deterioration similar to other TMOs. The 4MV electrode showed slightly improved stability; however, the performance was still unsatisfactory. The impurity phase in 4MV may lead to rapid capacity decay because it could hinder the Li^+ transport and cause uneven volume variation of the electrode upon charging/discharging.[63,64] A clear morphology re-construction of the 4MV electrode after cycling is evident in Figure 6c. The 4MMg electrode showed good cycling stability till ≈300 cycles. The inactive Mg spectator acted as a structural stabilizer, alleviating the electrode volume variation.[24] Nevertheless, a noticeable capacity degradation was still found if the cycle number further increased. As shown, the 4MCu electrode, even without any inactive component, exhibited almost no capacity decay after 400 cycles. The high phase purity of 4MCu maximizes the entropy stabilization effects that maintain the crystalline oxide framework and improve the electrochemical reversibility of the electrode.[14,23] Moreover, the high O_v content promotes phase change reversibility and reduces the

© 2022 Wiley-VCH GmbH

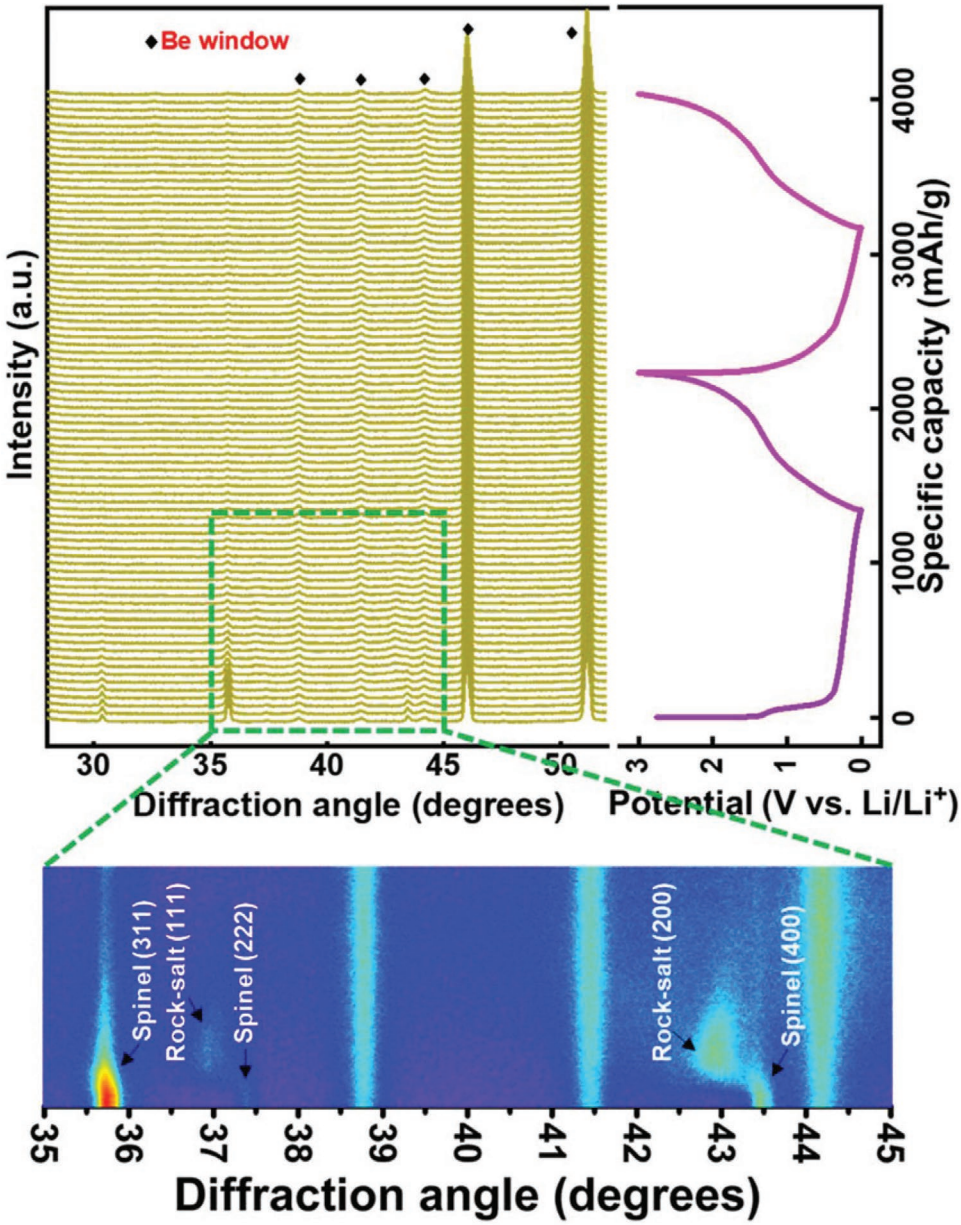

Figure 5. Operando XRD patterns of 4MCu electrode recorded during two charge–discharge cycles.

lattice stress during lithiation/delithiation.[65,66] Figure 6e confirms the great structural integrity of the 4MCu electrode after cycling, with the particle agglomeration and size expansion being limited compared to the other electrodes. The superior cyclability of this electrode is thus justified. As shown in Figure S5 (Supporting Information), capacity degradation of the 4MCu electrode is observed only after ≈440 cycles. The capacity retention after 500 cycles is ≈95%.

Figure 6f shows the EIS spectra of various electrodes after 400 cycles. The variations of the R_{ct} values for various electrodes are shown in Figure 6g. As summarized in Table 1, the significant deteriorations in R_{ct} and D_{Li^+} of the 4M and 4MV electrodes after cycling are noted. This is mainly associated with the electrode volume variation and morphology re-construction (Figure 6b,c), which lead to SEI accumulation. As a consequence, the redox charge transfer at the electrode interface and the Li^+ transport across SEI are hindered, resulting in the charge–discharge performance decay. The data in Table 1 also verify that a spectator element such as Mg is not necessary for achieving high cycling stability of a HESO electrode, given the chemical composition and phase purity are wisely controlled.

We speculate that the superior battery performance (great rate capability and negligible capacity decay after 400 cycles) of 4MCu is related to its stability of forming a single spinel phase. To understand the structural stability of 4M, 4MV, 4MMg, and 4MCu spinels, density functional theory calculations have been performed to compare their formation energies (see the details in Supporting Information). The optimized structures

 © 2022 Wiley-VCH GmbH

16163028, 2022, 17, Downloaded from https://onlinelibrary.wiley.com/doi/10.1002/adfm.202110992 by Massachusetts Institute of Technolo, Wiley Online Library on [31/07/2023]. See the Terms and Conditions (https://onlinelibrary.wiley.com/terms-and-conditions) on Wiley Online Library for rules of use; OA articles are governed by the applicable Creative Commons License

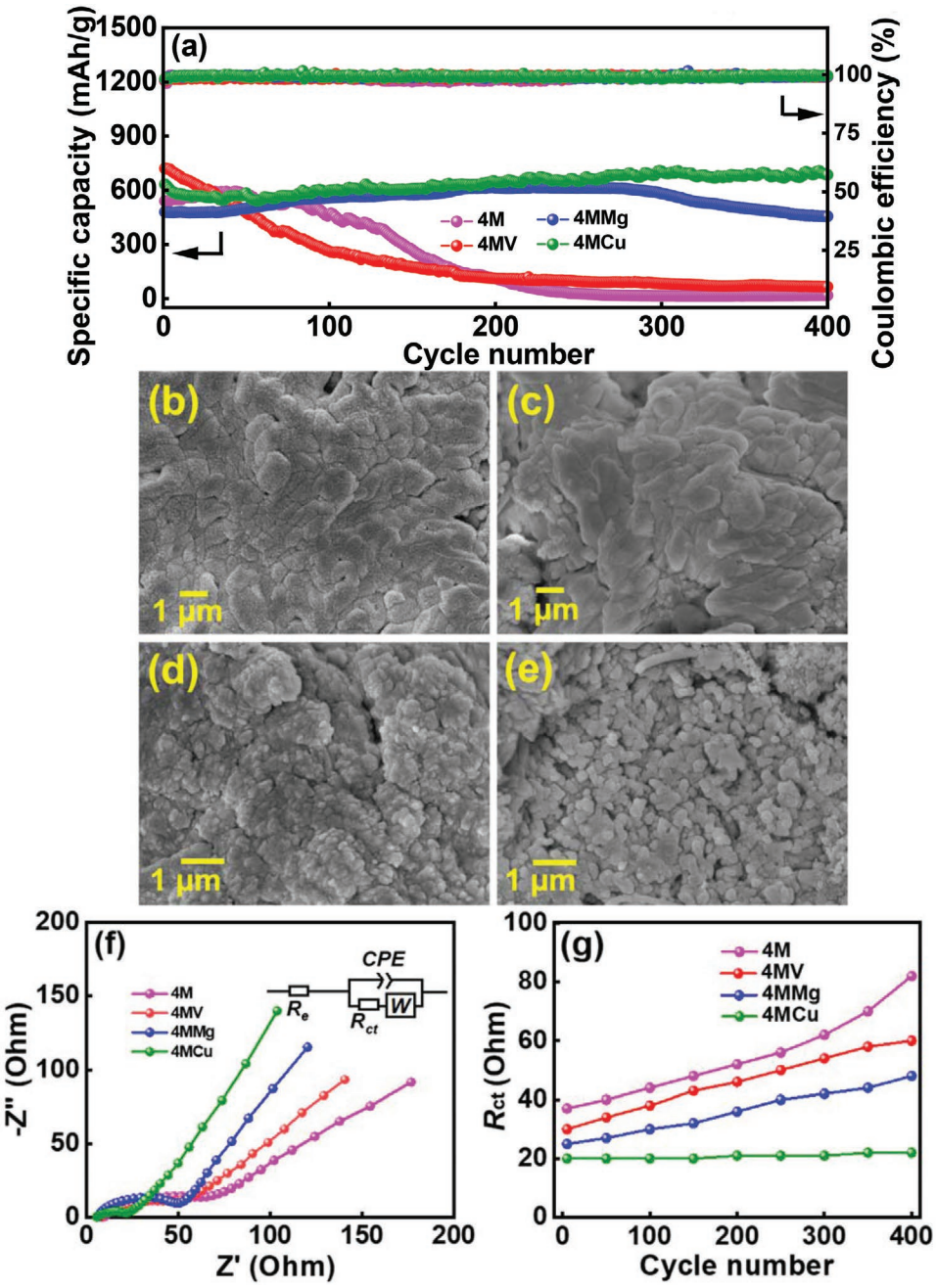

Figure 6. a) Cycling stability of various electrodes measured at 500 mA g^{-1} for 400 cycles. SEM images of b) 4M, c) 4MV, d) 4MMg, and e) 4MCu electrodes after cycling. f) EIS Nyquist spectra of various electrodes after cycling. g) Variations of R_{ct} values versus cycle number for various electrodes.

are illustrated in Figures S6–S9 (Supporting Information). Our computational outcomes indicate that 4MCu has the lowest formation energy (3.14 eV per formula unit), confirming its highest single-phase formation tendency among the samples.

The postmortem XPS analyses were performed for the 4MV, 4MMg, and 4MCu electrodes, and the data are shown in Figure S10 (Supporting Information). All the elements (except Mg^{2+}) have been partially reduced apart from the initial states, suggesting some irreversible reactions have occurred during cycling. In the Cr 2p spectra, the Cr^{6+} signals vanish and Cr^{3+} becomes dominant for all the samples. The 4MV even shows the presence of metallic Cr^0. The Mn spectra still exhibit both Mn^{2+} and Mn^{3+} states, whereas metallic Fe and Ni (besides 2+ and 3+ valences) are observed in all samples after cycling. It is noted that the Fe^0 and Ni^0 concentrations of 4MV are clearly higher than those of 4MMg and 4MCu. This indicates inferior redox reversibility of the 4MV electrode. The V 2p spectrum of 4MV shows a reduction of V^{5+}/V^{4+} to $V^{5+}/V^{4+}/V^{3+}$ after cycling. There is no binding energy change of the Mg 1s spectrum, confirming that Mg^{2+} is basically electrochemical inactive. In addition, mixed Cu^+/Cu^{2+} valence was observed for the cycled 4MCu. The Cu^+/Cu^{2+} ratio is slightly higher than that of the pristine electrode. As shown in the O 1s spectra, the O_V concentrations of all electrodes increase after cycling to maintain the charge balance.

© 2022 Wiley-VCH GmbH

16163028, 2022, 17, Downloaded from https://onlinelibrary.wiley.com/doi/10.1002/adfm.202110992 by Massachusetts Institute of Technolo, Wiley Online Library on [31/07/2023]. See the Terms and Conditions (https://onlinelibrary.wiley.com/terms-and-conditions) on Wiley Online Library for rules of use; OA articles are governed by the applicable Creative Commons License

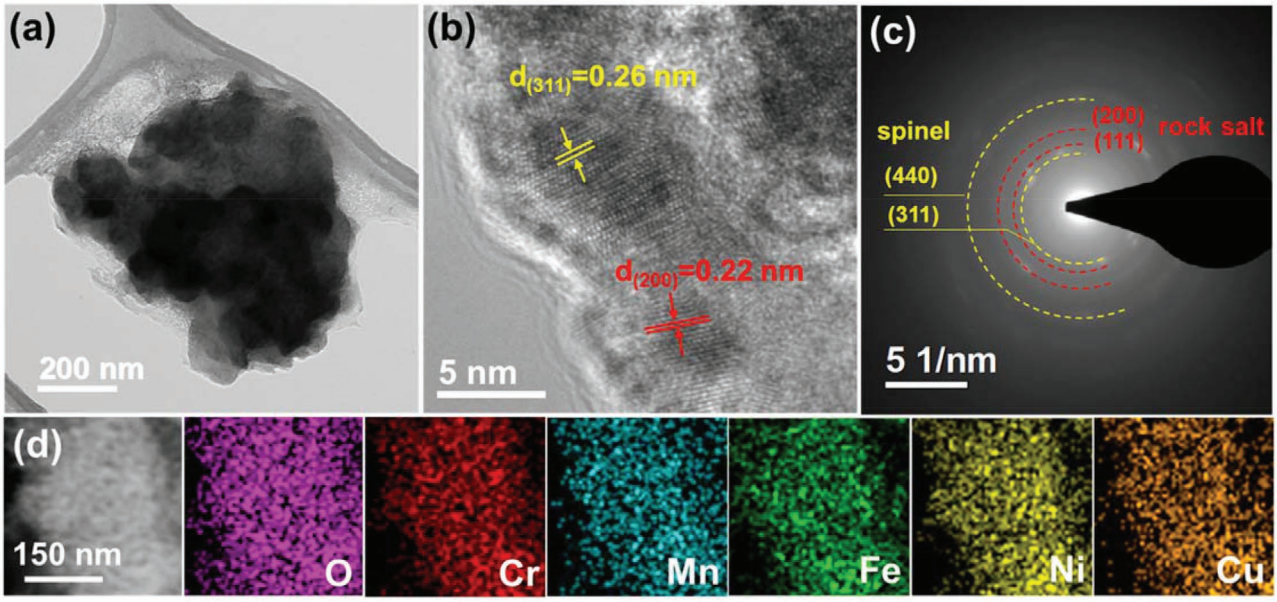

Figure 7. a) TEM image, b) high-resolution lattice image, c) SAED pattern, and d) HAADF image/EDS mapping data of 4MCu after 400 charge–discharge cycles.

Figure 7 shows the TEM analysis data of the 4MCu after cycling. The high-resolution TEM and SAED data confirm the existence of both crystalline spinel and rock-salt phases. The lattice fringes with *d* spacings of 0.26 and 0.22 nm were observed, which are attributed to (311) and (200) diffraction planes of spinel and rock-salt oxides, respectively. The preservation of the crystalline oxide structures after prolonged cycling is unique and can be ascribed to the entropy stabilization effects. For traditional TMO electrodes, the original crystallinity is totally lost after a few charge–discharge cycles.[9,67–70] As shown in Figure 7, all the elements are still uniformly distributed across the sample, suggesting that a high entropy state is well maintained. The superb conservation of the crystalline structure and elemental distribution contribute to the excellent cyclability of the 4MCu electrode.

As shown in Table S7 (Supporting Information), the proposed 4MCu electrode shows promising capacity, rate capability, and cycling stability among the reported HEO electrodes, especially compared to the Co-free samples. Therefore, the 4MCu‖$LiNi_{0.8}Co_{0.1}Mn_{0.1}O_2$ full cell was assembled, as depicted in **Figure 8**a, to evaluate the feasibility of the 4MCu electrode for practical battery applications. Figure 8b shows the charge-discharge profiles measured at various C-rates (1 C = 275 mAh g^{-1} for the cathode). The specific capacities are calculated based on the total mass of anode and cathode active materials. Accordingly, the energy density of the full cell (@0.1 C) is estimated to be ≈590 Wh kg^{-1} (based on electrode materials), which indicates the merit of the proposed anode material.

3. Conclusions

A series of Co-free HESO was successfully developed via a facile hydrothermal method. It was revealed that the phase purity of HESO, which was associated with the constituent elements, significantly affected the electrochemical lithiation/delithiation

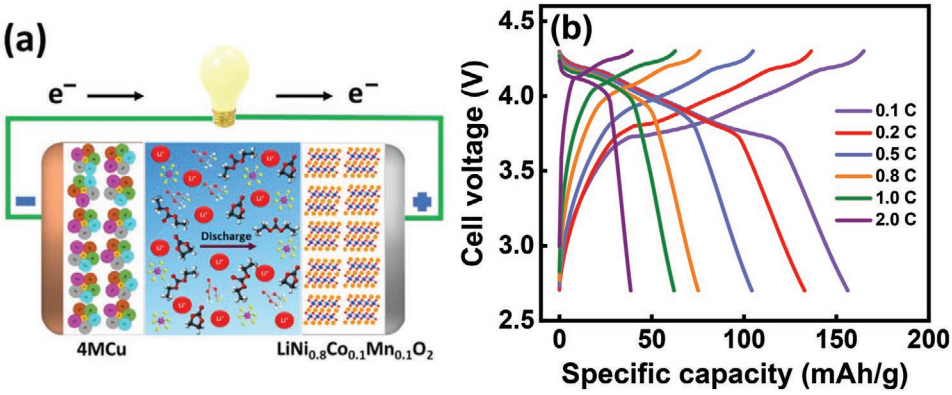

Figure 8. a) Scheme of LIB full cell with 4MCu anode and $LiNi_{0.8}Co_{0.1}Mn_{0.1}O_2$ cathode. b) Charge–discharge profiles of 4MCu‖ $LiNi_{0.8}Co_{0.1}Mn_{0.1}O_2$ full cell measured at various rates.

© 2022 Wiley-VCH GmbH

16163028, 2022, 17, Downloaded from https://onlinelibrary.wiley.com/doi/10.1002/adfm.202110992 by Massachusetts Institute of Technolo, Wiley Online Library on [31/07/2023]. See the Terms and Conditions (https://onlinelibrary.wiley.com/terms-and-conditions) on Wiley Online Library for rules of use; OA articles are governed by the applicable Creative Commons License

properties. Although V alloying increased specific capacity, it caused the formation of a large fraction of the $Mn_2V_2O_7$ impurity phase, leading to inferior rate capability and cycling stability of the electrode. In contrast, the high phase purity of 4MCu maximized the entropy stabilization effects that sustained the crystalline framework and promoted electrode reversibility. Moreover, the incorporated Cu existed in a Cu^+/Cu^{2+} mixed state and thus increased the O_V concentration, which was crucial to improving the rate capability and stability of the 4MCu electrode. Without having an inactive spectator element (such as Mg), the 4MCu exhibited almost no capacity decay after 400 charge–discharge cycles. According to the operando XRD analysis, a spinel-to-rock salt phase transition was observed for 4MCu before the formation of short-range ordered nano-crystals during the first lithiation. The nano-crystalline nature was preserved upon delithiation. The 4MCu‖$LiNi_{0.8}Co_{0.1}Mn_{0.1}O_2$ full cell showed a promising energy density. This paper emphasizes that the elemental design criteria for HESO should consider the phase purity and O_v content for achieving superior LIB performance.

4. Experimental Section

Material Synthesis: The samples were prepared using a hydrothermal method. Equimolar (1 mmol) $Cr(NO_3)_3{\cdot}9H_2O$ (Alfa Aesar, 98.5%), $Mn(NO_3)_2{\cdot}6H_2O$ (Alfa Aesar, 98.5%), $Fe(NO_3)_3{\cdot}9H_2O$ (J.T. Baker, 99%), and $Ni(NO_3)_2{\cdot}6H_2O$ (Alfa Aesar, 98.5%) were dissolved in 40 mL de-ionized (DI) water, followed by the addition of 1.25 mmol (1-hexadecyl)trimethylammonium bromide (Alfa Aesar, 98.5%). The resulting solution was stirred for homogeneity, and then urea was added, with urea to total metal precursor molar ratio of 6:1. Afterward, the solution was transferred to a Teflon-lined stainless-steel autoclave and heated at 140 °C for 5 h. After cooling, the product was collected through centrifugation, washed with ethanol and DI water, filtered, and dried in a vacuum oven at 60 °C overnight. The obtained powder was heated in air at a rate of 6 °C min^{-1} to 900 °C and dwelled for 2 h. This sample is designated as 4M. The 5-cation 4MV, 4MMg, and 4MCu samples were prepared using the same method, in which 1 mmol NH_4VO_3, 1 mmol $Mg(NO_3)_2{\cdot}6H_2O$, and 2 mmol $Cu(NO_3)_2{\cdot}2.5H_2O$ were added, respectively.

Material Characterizations: The crystallinity of the samples was characterized using XRD (Bruker D8 Discover with a Cu Kα X-ray source). The diffraction angle was scanned from 10° to 80° with a speed of 2° min^{-1}. The oxide morphology was examined using (SEM, JEOL 6701F). TEM (JEOL JEM-2100F), EDS, and SAED were employed to study the material microstructures, chemical compositions, and crystal structures, respectively. The valence states of the samples were investigated using (XPS Versaprobe PHI 5000). The data fitting was conducted using XPSPEAK 4.1 software. All the XPS spectra were calibrated with the binding energy of C 1s electron at 284.8 eV. ICP-MS, (Thermo-Element XR) was utilized to quantify the constituent elements of the samples.

Electrochemical Measurements: The electrode preparation and cell assembly details are described in Supporting Information. The EIS data were recorded within 10^6–10^{-2} Hz. The capacities, capability performance, and cycling stability of various cells were studied at 25 °C using an Arbin battery tester. To construct a 4MCu‖$LiNi_{0.8}Co_{0.1}Mn_{0.1}O_2$ full cell, an anode-to-cathode capacity ratio of 1.2 was used. The 4MCu anode was preconditioned and lithiated by 20% in a half cell prior to the full cell assembly. For each testing condition, at least five duplicate cells were measured. The performance deviation was typically within 5%. The reported data were the median values. A Bruker D2 diffractometer was used to collect the operando XRD patterns between 0.01 and 3.0 V (vs Li/Li^+). The charge–discharge specific current was 200 mA g^{-1}.

Supporting Information

Supporting Information is available from the Wiley Online Library or from the author.

Acknowledgements

J.P., T.X.N., and C.-C.T. contributed equally to this work. The financial support provided for this work by the Ministry of Science and Technology (MOST) of Taiwan is gratefully appreciated. W.K.C., C.-H.L., and H.-Y.T.C. thank MOST in Taiwan (108-2112-M-007-023-MY3) for the financial support. The computing resources were supported by TAIWANIA in National Center for High-Performance Computing (NCHC) in Taiwan.

Conflict of Interest

The authors declare no conflict of interest.

Data Availability Statement

The data that support the findings of this study are available from the corresponding author upon reasonable request.

Keywords

chemical composition, cycling stability, entropy stabilization effects, full cell performance, high capacity, in operando X-ray diffraction

Received: October 30, 2021
Revised: December 31, 2021
Published online: February 1, 2022

[1] C. P. Grey, D. S. Hall, *Nat. Commun.* **2020**, *11*, 6279.
[2] A. Manthiram, *Nat. Commun.* **2020**, *11*, 1550.
[3] J. Asenbauer, T. Eisenmann, M. Kuenzel, A. Kazzazi, Z. Chen, D. Bresser, *Sustainable Energy Fuels* **2020**, *4*, 5387.
[4] M. V. Reddy, G. V. Subba Rao, B. V. R. Chowdari, *Chem. Rev.* **2013**, *113*, 5364.
[5] S. Fang, D. Bresser, S. Passerini, *Adv. Energy Mater.* **2020**, *10*, 1902485.
[6] R. Chen, R. Luo, Y. Huang, F. Wu, L. Li, *Adv. Sci.* **2016**, *3*, 1600051.
[7] J. Cabana, L. Monconduit, D. Larcher, M. R. Palacin, *Adv. Mater.* **2010**, *22*, E170.
[8] Y. Lu, L. Yu, X. W. Lou, *Chem* **2018**, *4*, 972.
[9] S. H. Yu, S. H. Lee, D. J. Lee, Y. E. Sung, T. Hyeon, *Small* **2016**, *12*, 2146.
[10] Y. H. Kwon, K. Minnici, M. M. Huie, K. J. Takeuchi, E. S. Takeuchi, A. C. Marschilok, E. Reichmanis, *Chem. Mater.* **2016**, *28*, 6689.
[11] N. Nitta, F. Wu, J. T. Lee, G. Yushin, *Mater. Today* **2015**, *18*, 252.
[12] A. Sarkar, Q. Wang, A. Schiele, M. R. Chellai, S. S. Bhattacharya, D. Wang, T. Brezesinski, H. Hahn, L. Velasco, B. Breitung, *Adv. Mater.* **2019**, *31*, 1806236.
[13] A. Amiri, R. S. Yassar, *J. Mater. Chem. A.* **2021**, *9*, 782.
[14] Y. Ma, Y. Ma, Q. Wang, S. Schweidler, M. Botros, T. Fu, H. Hahn, T. Brezensinki, B. Beritung, *Energy Environ. Sci.* **2021**, *14*, 2883.
[15] C. M. Rost, E. Sachet, T. Borman, A. Moballegh, E. C. Dickey, D. Hou, J. L. Jones, S. Curtarolo, J. P. Maria, *Nat. Commun.* **2015**, *6*, 8485.
[16] M. Fu, X. Ma, K. Zhao, X. Li, D. Su, *iScience* **2021**, *24*, 102177.

© 2022 Wiley-VCH GmbH

16163028, 2022, 17, Downloaded from https://onlinelibrary.wiley.com/doi/10.1002/adfm.202110992 by Massachusetts Institute of Technolo, Wiley Online Library on [31/07/2023]. See the Terms and Conditions (https://onlinelibrary.wiley.com/terms-and-conditions) on Wiley Online Library for rules of use; OA articles are governed by the applicable Creative Commons License

[17] T. X. Nguyen, Y. C. Liao, C. C. Lin, Y. H. Su, J. M. Ting, *Adv. Funct. Mater.* **2021**, *31*, 2101632.
[18] D. Berardan, S. Franger, D. Dragoe, A. K. Menna, N. Dragoe, *Phys. Status Solidi RRL* **2016**, *10*, 328.
[19] A. Sarkar, R. Kruk, H. Hahn, *Dalton Trans.* **2021**, *50*, 1973.
[20] A. Sarkar, C. Loho, L. Velasco, T. Thomas, S. S. Bhattacharya, H. Hahn, R. Djenadic, *Dalton Trans.* **2017**, *46*, 12167.
[21] S. Zhai, J. Rojas, N. Ahlborg, K. Lim, M. F. Toney, H. Jin, W. C. Chueh, A. Majumdar, *Energy Environ. Sci.* **2018**, *11*, 2172.
[22] D. B. Miracle, O. N. Senkov, *Acta Mater.* **2017**, *122*, 448.
[23] A. Sarkar, L. Velasco, D. Wang, Q. Wang, G. Talasila, L. de Biasi, C. Kübel, T. Brezesinski, S. S. Bhattacharya, H. Hahn, B. Breitung, *Nat. Commun.* **2018**, *9*, 3400.
[24] N. Qiu, H. Chen, Z. Yang, S. Sun, Y. Wang, Y. Cui, *J. Alloys Compd.* **2019**, *777*, 767.
[25] P. Ghigna, L. Airoldi, M. Fracchia, D. Callegari, U. A. Tamburini, P. D'Angelo, N. Pianta, R. Ruffo, G. Cibin, D. O. de Souza, E. Quartarone, *ACS Appl. Mater. Interfaces* **2020**, *12*, 50344.
[26] T. X. Nguyen, J. Patra, J. K. Chang, J. M. Ting, *J. Mater. Chem. A* **2020**, *8*, 18963.
[27] C. Y. Huang, C. W. Huang, M. C. Wu, J. Patra, T. X. Nguyen, M. T. Chang, O. Clemens, J. M. Ting, J. Li, J. K. Chang, *Chem. Eng. J.* **2021**, *420*, 129838.
[28] T. Y. Chen, S. Y. Wang, C. H. Kuo, S. C. Huang, M. H. Lin, C. H. Li, H. Y. T. Chen, C. C. Wang, Y. F. Liao, C. C. Lin, Y. M. Chang, J. W. Yeh, S. J. Lin, T. Y. Chen, H. Y. Chen, *J. Mater. Chem. A* **2020**, *8*, 21756.
[29] M. Li, J. Lu, *Science* **2020**, *367*, 979.
[30] W. Li, S. Lee, A. Manthiram, *Adv. Mater.* **2020**, *32*, 2002718.
[31] Y. Ma, Y. Ma, S. L. Dreyer, Q. Wang, K. Wang, D. Goonetilleke, A. Omar, D. Mikhailova, H. Hahn, B. Breitung, T. Bewzesinki, *Adv. Mater.* **2021**, *33*, 2101342.
[32] C. Duan, K. Tian, X. Li, D. Wang, H. Sun, R. Zheng, Z. Wang, Y. Liu, *Ceram. Int.* **2021**, *47*, 32025.
[33] B. Xiao, G. Wu, T. Wang, Z. Wei, Y. Sui, B. Shen, J. Qi, F. Wei, Q. Meng, Y. Ren, X. Xue, J. Zheng, J. Mao, K. Dai, *Ceram. Int.* **2021**, *47*, 33972.
[34] D. C. Kim, S. K. Ihm, *Environ. Sci. Technol.* **2001**, *35*, 226.
[35] J. Słoczyński, J. Janas, T. Machej, J. Rynkowski, J. Stoch, *Appl. Catal. B: Environ.* **2000**, *24*, 45.
[36] J. Zhang, R. Chu, Y. Chen, Y. Zeng, Y. Zhang, H. Guo, *Electrochim. Acta* **2019**, *319*, 518.
[37] T. Yamashita, P. Hayes, *Appl. Surf. Sci.* **2008**, *254*, 2441.
[38] A. P. Grosvenor, B. A. Kobe, M. C. Biesinger, N. S. McIntyre, *Surf. Interface Anal.* **2004**, *36*, 1564.
[39] Z. Fu, J. Hu, W. Hu, S. Yang, Y. Luo, *Appl. Surf. Sci.* **2018**, *441*, 1048.
[40] L. Ma, S. S. Lyu, Y. Dai, X. Y. Pei, D. C. Mo, Y. X. Fu, *J. Alloys Compd.* **2019**, *810*, 151954.
[41] H. Zhou, F. Yu, Q. Zhu, J. Sun, F. Qin, L. Yu, J. Bao, Y. Yu, S. Chen, Z. Ren, *Energy Environ. Sci.* **2018**, *11*, 2858.
[42] F. Lei, Y. Sun, K. Liu, S. Gao, L. Liang, B. Pan, Y. Xie, *J. Am. Chem. Soc.* **2014**, *136*, 6826.
[43] T. X. Nguyen, Z. T. Huang, J. M. Ting, *Appl. Surf. Sci.* **2021**, *570*, 151160.
[44] H. Z. Xiang, H. X. Xie, X. X. Chen, H. Zhang, A. Mao, C. H. Zheng, *J. Mater. Sci.* **2021**, *56*, 8127.
[45] Q. Wang, A. Sarkar, D. Wang, L. Velasco, R. Azmi, S. S. Bhattacharya, T. Bergfeldt, A. Duvel, P. Heitjans, T. Brezesinski, H. Hahn, B. Breitung, *Energy Environ. Sci* **2019**, *12*, 2433.
[46] D. Puthusseri, M. Wahid, S. Ogale, *ACS Omega* **2018**, *3*, 4591.
[47] Q. Xia, D. M. Avdeev, S. Schmid, H. Liu, B. Johannessen, C. D. Ling, *Batteries Supercaps* **2021**, *4*, 195.
[48] P. Li, Y. Liu, J. Liu, Z. Li, G. Wu, M. Wu, *Chem. Eng. J.* **2015**, *271*, 173.
[49] S. F. Zheng, J. S. Hu, L. S. Zhong, W. G. Song, L. J. Wan, Y. G. Guo, *Chem. Mater.* **2008**, *20*, 3617.
[50] F. Han, W. Cui, D. Li, A. H. Lu, *ChemElectroChem* **2014**, *1*, 733.
[51] F. Zheng, D. Zhu, Q. Chen, *ACS Appl. Mater. Interface* **2014**, *6*, 9256.
[52] W. Zhou, J. Zhu, C. Cheng, J. Liu, H. Yang, C. Cong, C. Guan, X. Jia, H. J. Fan, Q. Yan, C. M. Li, T. Yu, *Energy Environ. Sci.* **2011**, *4*, 4954.
[53] Z. Zhang, Y. Ji, J. Li, Q. Tan, Z. Zhong, F. Su, *ACS Appl. Mater. Interfaces* **2015**, *7*, 6300.
[54] H. Chen, N. Qiu, B. Wu, Z. Yang, S. Sun, Y. Wang, *RSC Adv.* **2020**, *10*, 9736.
[55] D. Wang, S. Jiang, C. Duan, J. Mao, Y. Dong, K. Dong, Z. Wang, S. Luo, Y. Liu, X. Qi, *J. Alloys Compd.* **2020**, *844*, 156158.
[56] J. Garche, C. K. Dyer, P. T. Moseley, Z. Ogumi, D. A. J. Rand, B. Scrosati, *Encyclopedia of Electrochemical Power Sources*, Elsevier Science, Amsterdam, the Netherlands **2009**.
[57] P. Spies, M. Pollak, L. Mateu, *Handbook of Energy Harvesting Power Supplies and Applications*, CRC Press, Taylor & Francis Group, Boca Raton, FL **2013**.
[58] J. Patra, H. T. Huang, W. Xue, C. Wang, A. S. Helal, J. Li, J. K. Chang, *Energy Storage Mater.* **2019**, *16*, 146.
[59] J. Patra, P. C. Rath, C. Li, H. M. Kao, F. M. Wang, J. Li, J. K. Chang, *ChemSusChem* **2018**, *11*, 3923.
[60] J. Patra, S. C. Wu, I. C. Lue, C. C. Yang, R. S. Dhaka, S. Okada, H. L. Yeh, C. M. Hsieh, B. K. Chang, J. K. Chang, *ACS Appl. Energy Mater.* **2021**, *4*, 5738.
[61] Y. Zou, W. Zhang, N. Chen, S. Chen, W. Xu, R. Cai, C. L. Brown, D. Yang, X. Yao, *ACS Nano* **2019**, *13*, 2062.
[62] E. Uchaker, Y. Z. Zheng, S. Li, S. L. Candelaria, S. Hu, G. Z. Cao, *J. Mater. Chem. A* **2014**, *2*, 18208.
[63] T. X. Nguyen, C. C. Tsai, J. Patra, O. Clemens, J. K. Chang, J. M. Ting, *Chem. Eng. J.* **2020**, *430*, 132658.
[64] N. D. Rosedhi, N. H. Idris, M. M. Rahman, M. F. M. Din, J. Wang, *Electrochim. Acta* **2016**, *206*, 374.
[65] Q. Li, D. Ning, D. Zhou, K. An, D. Wong, L. Zhang, Z. Chen, G. Schuck, C. Schultz, Z. Xu, G. Schumacher, X. Liu, *J. Mater. Chem. A* **2020**, *8*, 7733.
[66] W. Ma, C. Zhang, C. Liu, X. Nan, H. Fu, G. Cao, *ACS Appl. Mater. Interfaces* **2016**, *8*, 19542.
[67] N. Spinner, L. Zhang, W. E. Mustain, *J. Mater. Chem. A* **2014**, *2*, 1627.
[68] R. Cai, S. Guo, Q. Meng, S. Yang, H. L. Xin, M. Li, Y. Sun, P. Gao, S. Zhang, H. Dong, S. Lei, K. Kim, H. Zeng, L. Sun, F. Xu, Y. Zhu, *Nano Energy* **2019**, *63*, 103840.
[69] K. Cao, L. Jiao, H. Liu, Y. Liu, Y. Wang, Z. Guo, H. Yuan, *Adv. Energy Mater.* **2015**, *5*, 1401421.
[70] L. Luo, J. Wu, J. Xu, V. P. Dravid, *ACS Nano* **2014**, *8*, 11560.

© 2022 Wiley-VCH GmbH

16163028, 2022, 17, Downloaded from https://onlinelibrary.wiley.com/doi/10.1002/adfm.202110992 by Massachusetts Institute of Technolo, Wiley Online Library on [31/07/2023]. See the Terms and Conditions (https://onlinelibrary.wiley.com/terms-and-conditions) on Wiley Online Library for rules of use; OA articles are governed by the applicable Creative Commons License

ADVANCED FUNCTIONAL MATERIALS

Supporting Information

for *Adv. Funct. Mater.,* DOI: 10.1002/adfm.202110992

Effects of Elemental Modulation on Phase Purity and Electrochemical Properties of Co-free High-Entropy Spinel Oxide Anodes for Lithium-Ion Batteries

Jagabandhu Patra, Thi Xuyen Nguyen, Chia-Chien Tsai, Oliver Clemens, Ju Li, Pratibha Pal, Weng Kent Chan, Chih-Heng Lee, Hsin-Yi Tiffany Chen, Jyh-Ming Ting, and Jeng-Kuei Chang**

Copyright WILEY-VCH GmbH 2022.

Supporting Information

Effects of Elemental Modulation on Phase Purity and Electrochemical Properties of Co-free High-Entropy Spinel Oxide Anodes for Lithium-Ion Batteries

Jagabandhu Patra[#], Thi Xuyen Nguyen[#], Chia-Chien Tsai[#], Oliver Clemens, Ju Li, Pratibha Pal, Weng Kent Chan, Chih-Heng Lee, Hsin-Yi Tiffany Chen, Jyh-Ming Ting, Jeng-Kuei Chang**

Electrode preparation and cell assembly

To prepare the electrode, a slurry made out of 70 wt% active material, 20 wt% Super P, and 10 wt% sodium polyacrylate binder in DI water was coated on Cu foil using a doctor blade. The obtained electrodes were vacuum-dried at 80 °C for 8 h, roll-pressed, and then punched to match the required dimensions of a CR2032 coin cell. The active material loading was ~2 mg cm^{-2}. Li foil and a glass fiber membrane were used as the counter electrode and separator, respectively. The electrolyte was composed of 1 M $LiPF_6$ salt, ethylene carbonate/diethyl carbonate (1:1 by volume) mixed solvent, and 5 wt% fluoroethylene carbonate additive. Assembly of the coin cells was performed in an argon-filled glove box (Vigor Tech. Co. Ltd.), where both the moisture and oxygen content levels were maintained at below 0.2 ppm.

Density functional theory calculation

Special Quasirandom Structure (SQS) algorithm[1] implanted in the mcsqs code[2] has been applied to obtain the initial four high-entropy oxide materials (4M, 4MV, 4MMg, and 4MCu) with a spinel structure. To understand their structural stability, spin-polarized density functional theory (DFT)[3] calculation has been performed by using Vienna Ab initio Simulation Package (VASP).[4] Projector augmented wave pseudopotential [5,6] and Perdew-Burke-Ernzerhof (PBE)[7] exchange-correlation functional were used with considering Hubbard correction; their effective on-site Coulomb and exchange parameters, U (eV) and J (eV) values, are listed in the table below. Electron density and ground state energy were calculated by setting the plane-wave basis with an energy cutoff of 500 eV. The structures were optimized using a conjugated-gradient algorithm until the ionic forces were smaller than 0.01 eV/Å and energy had converged within 0.00001eV. Γ-centered k-point mesh of 2 × 2 × 2 was applied to optimize these four models.

Table. Hubbard correction terms, U (eV) and J (eV), of DFT calculation used in this work.

Reference	Element	U (eV)	J (eV)
8	Cr	3.0	0.87
9	Ni	8.0	0.95
9	Mn	6.9	0.86
9	Fe	6.8	0.89
9	V	6.7	0.81
9	Cu	7.5	0.98

References:

1. A. Zunger, S. H. Wei, L. G. Ferreira, J. E. Bernard, *Phys. Rev. Lett.* **1990**, *65*, 353.
2. A. V. D. Walle, P. Tiwary, M. D. Jong, D. L. Olmsted, M. Asta, A. Dick, D. Shin, Y. Wang, L. Q. Chen, Z. K. Liu, *Calphad* **2013**, *42*, 13.
3. P. Hohenberg, W. Kohn, *Phys. Rev*. **1964**, *136*, B864.

4. G. Kresse, J. Furthmüller, *Comput. Mater. Sci.* 1996, **6**, 15.
5. P. E. Blöchl, *Phys. Rev. B* **1994**, *50*, 17953.
6. G. Kresse, D. Joubert, Phys. Rev. B **1999**, *59***,** 1758.
7. J. P. Perdew, K. Burke, M. Ernzerhof, Phys. Rev. Lett. **1996**, ***77***, 3865.
8. M. A. Korotin, V. I. Anisimov, D. I. Khomskii, G. A. Sawatzky, *Phys. Rev. Lett*. **1998**, *80*, 4305.
9. V. I. Anisimov, J. Zaanen, O. K. Andersen, *Phys. Rev. B* **1991**, *44*, 943.

Table. Formation energy, E_{form} (eV/formula unit), of four models of high-entropy spinel oxide materials (4M, 4MV, 4MMg, and 4MCu) calculated by DFT.

Material	E_{form} (eV/formula unit)
4M	4.44
4MV	4.65
4MMg	6.91
4MCu	3.14

Table S1. Rietveld refinement results of 4M sample. The R_{exp}, R_{wp}, and R_p values are 66.8, 55.1, and 48.7, respectively.

Sample ID	**4M**		
Phase	Spinel	Spinel	Bixbyite
R-Bragg	13.804	26.056	29.831
Space-group	Fd-3m	Fd-3m	Ia-3
Wt% - Rietveld	86.1 %	9.4 %	4.5 %
Cell volume ($Å^3$)	572.8(3)	600.1(4)	827.9(5)
Crystal Density (g cm^{-3})	5.335(3)	5.092(4)	5.066(3)
Lattice parameter (Å)	8.3051(13)	8.435(2)	9.390(2)

Table S2. Rietveld refinement results of 4MV sample. The R_{exp}, R_{wp}, and R_p values are 6.7, 5.7, and 4.4, respectively.

Sample ID	**4MV**	
Phase	Spinel	$Mn_2V_2O_7$
R-Bragg	2.904	1.651
Space-group	*Fd-3m*	*C12/m1*
Wt% - Rietveld	75.5 %	24.5 %
Cell volume ($Å^3$)	577.97(16)	281.9(4)
Crystal Density (g cm^{-3})	5.0974(14)	3.814(6)
Lattice parameter (Å)	8.3298(8)	a=6.800(5) b=8.653(8) c=4.946(5) α=90° β=104.39° γ=90°

Table S3. Rietveld refinement results of 4MMg sample. The R_{exp}, R_{wp}, and R_p values are 7.0, 5.8, and 4.4, respectively.

Sample ID	**4MMg**	
Phase	Spinel	Rock Salt
R-Bragg	2.904	3.943
Space-group	*Fd-3m*	*Fm-3m*
Wt% - Rietveld	86.3 %	13.7 %
Cell volume ($Å^3$)	579.3(2)	73.48(7)
Crystal Density (g cm^{-3})	4.8553(18)	6.752(6)
Lattice parameter (Å)	8.3360(10)	4.1885(13)

Table S4. Rietveld refinement results of 4MCu sample. The R_{exp}, R_{wp}, and R_p values are 6.5, 4.9, and 3.8, respectively.

Sample ID	**4MCu**
Phase	Spinel
R-Bragg	2.432
Space-group	Fd-3m
Wt% - Rietveld	100 %
Cell volume ($Å^3$)	575.70(16)
Crystal Density (g cm^{-3})	5.3941(15)
Lattice parameter (Å)	8.3189(8)

Table S5. ICP-MS results and calculated configurational entropy values of 4M, 4MV, 4MMg, and 4MCu samples.

ID	Cr%	Mn%	Fe%	Ni%	V%	Mg%	Cu%	$S_{config.}$
4M	26.31	25.59	21.75	26.35	-	-	-	1.383 *R*
4MV	21.20	20.22	17.70	20.33	20.55	-	-	1.608 *R*
4MMg	20.68	18.16	21.52	19.94	-	19.70	-	1.608 *R*
4MCu	23.48	19.58	18.69	23.09	-	-	15.16	1.600 *R*

Table S6. Specific capacities of various electrodes measured at different rates.

	Reversible capacity (mAh/g)			
Specific current (mA/g)	4M	4MV	4MMg	4MCu
50	750	1005	590	800
100	658	932	562	760
200	602	837	538	704
500	543	729	484	647
800	465	640	453	593
1000	404	597	436	556
1500	345	500	400	510
2000	300	442	342	480

Table S7. Comparison of capacities, rate capability, and cycling stability of our 4MCu electrode and various HEO electrodes reported in the literature.

Material	Low-rate performance	High-rate performance	Cycling stability	Reference
(**Co**$_{0.2}$Cu$_{0.2}$Mg$_{0.2}$Ni$_{0.2}$Zn$_{0.2}$)O	~600 mAh g^{-1} @ 50 mAg^{-1}	~160 mAh g^{-1} @ 3000 mAg^{-1}	100 % after 300 cycles @ 200 mA hg^{-1}	10
Mg$_{0.2}$**Co**$_{0.2}$Ni$_{0.2}$Cu$_{0.2}$Zn$_{0.2}$O	955 mAh g^{-1} @ 100 mAg^{-1}	490 mAh g^{-1} @ 3000 mAg^{-1}	100 % after 300 cycles @ 100 mA hg^{-1}	11
(Mg$_{0.2}$**Co**$_{0.2}$Ni$_{0.2}$Cu$_{0.2}$Zn$_{0.2}$)O	829 mAh g^{-1} @ 100 mAg^{-1}	408 mAh g^{-1} @ 2000 mAg^{-1}	~100 % after 150 cycles @ 200 mA hg^{-1}	12
(Mg**Co**NiZn)$_{0.65}$Li$_{0.35}$O	925 mAh g^{-1} @ 100 mAg^{-1}	610 mAh g^{-1} @ 1000 mAg^{-1}	~85 % after 100 cycles @ 1000 mA hg^{-1}	13
Mg$_{0.2}$**Co**$_{0.2}$Ni$_{0.2}$Cu$_{0.2}$Zn$_{0.2}$O	~600 mAh g^{-1} @ 89 mAg^{-1}	~300 mAh g^{-1} @ 1800 mAg^{-1}	NA	14
(Ni$_{0.2}$**Co**$_{0.2}$Mn$_{0.2}$Fe$_{0.2}$Ti$_{0.2}$)$_3$O$_4$	594 mAh g^{-1} @ 50 mAg^{-1}	343 mAh g^{-1} @ 2500 mAg^{-1}	~100 % after 100 cycles @ 100 mA hg^{-1}	15
(**Co**CrMnFeNi)$_3$O$_4$	1235 mAh g^{-1} @ 20 mAg^{-1}	500 mAh g^{-1} @ 2000 mAg^{-1}	90 % after 200 cycles @ 500 mA hg^{-1}	16
(Fe**Co**NiCrMn)$_3$O$_4$	735 mAh g^{-1} @ 50 mAg^{-1}	180 mAh g^{-1} @ 2000 mAg^{-1}	~80 % after 300 cycles @ 50 mA hg^{-1}	17
(Fe**Co**NiCrMnZnLi)$_3$O$_4$	695 mAh g^{-1} @ 50 mAg^{-1}	173 mAh g^{-1} @ 2000 mAg^{-1}	~80 % after 100 cycles @ 500 mA hg^{-1}	18
(Al$_{0.2}$**Co**CrFeMnNi)$_{0.58}$O$_{4-\delta}$	~1400 mAh g^{-1} @ 100 mAg^{-1}	634 mAh g^{-1} @ 3000 mAg^{-1}	~40 % after 500 cycles @ 200 mA hg^{-1}	19
(MgCuNi**Co**Zn)O	~400 mAh g^{-1} @ 100 mAg^{-1}	250 mAh g^{-1} @ 5000 mAg^{-1}	~100 % after 1000 cycles @ 200 mA hg^{-1}	20
(**Co**CuMgNiZn)O	477 mAh g^{-1} @ 100 mAg^{-1}	240 mAh g^{-1} @ 2000 mAg^{-1}	92 % after 200 cycles @ 120 mA hg^{-1}	21
(**Co**CrMnFeNi)$_3$O$_4$	1225 mAh g^{-1} @ 20 mAg^{-1}	485 mAh g^{-1} @ 2000 mAg^{-1}	91 % after 200 cycles @ 500 mA hg^{-1}	22
(**Co**$_{0.2}$Cr$_{0.2}$Fe$_{0.2}$Mn$_{0.2}$Ni$_{0.2}$)$_3$O$_4$	~863 mAh g^{-1} @ 100 mAg^{-1}	~430 mAh g^{-1} @ 10000 mAg^{-1}	100 % after 50 cycles @ 100 mA hg^{-1}	23
Co-free HEOs below				
(FeNiCrMnZn)$_3$O$_4$	692 mAh g^{-1} @ 100 mAg^{-1}	260 mAh g^{-1} @ 3000 mAg^{-1}	~85 % after 100 cycles @ 500 mA hg^{-1}	24
(Mg$_{0.2}$Ti$_{0.2}$Zn$_{0.2}$Cu$_{0.2}$Fe$_{0.2}$)$_3$O$_4$	571 mAh g^{-1} @ 100 mAg^{-1}	268 mAh g^{-1} @ 2000 mAg^{-1}	~87 % after 300 cycles @ 100 mA hg^{-1}	25
(CrMnFeNiCu)$_3$O$_4$	755 mAh g^{-1} @ 50 mAg^{-1}	451 mAh g^{-1} @ 2000 mAg^{-1}	99 % after 250 cycles @ 500 mA hg^{-1}	26
(CrMnFeNiCu)$_3$O$_4$	800 mAh g^{-1} @ 50 mAg^{-1}	480 mAh g^{-1} @ 2000 mAg^{-1}	100 % after 400 cycles @ 500 mA hg^{-1}	This work

References:

10. A. Sarkar, L. Velasco, D. Wang, Q. Wang, G. Talasila, L. de Biasi, C. Kübel, T. Brezesinski, S. S. Bhattacharya, H. Hahn, B. Breitung, *Nat. Commun*. **2018**, *9*, 3400.
11. N. Qiu, H. Chen, Z. Yang, S. Sun, Y. Wang, Y. Cui, *J. Alloys Compd*. **2019**, *777*, 767.
12. H. Chen, N. Qiu, B. Wu, Z. Yang, S. Sun, Y. Wang, *RSC Adv*. **2019**, *9*, 28908.
13. E. Lokcu, C. Toparli, M. Anik, *ACS Appl. Mater. Interface* **2020**, *12*, 23860.
14. P. Ghigna, L. Airoldi, M. Fracchia, D. Callegari, U. A.Tamburini, P. D'Angelo, N. Pianta, R. Ruffo, G. Cibin, D.O. de Souza, E. Quartarone, *ACS Appl. Mater. Interfaces* **2020**, *12*, 50344.
15. T. Y. Chen, S. Y. Wang, C. H. Kuo, S. C. Huang, M. H. Lin, C. H. Li, H. Y. T. Chen, C. C. Wang, Y. F. Liao, C. C. Lin, Y. M. Chang, J. W. Yeh, S. J. Lin, T. Y. Chen, H. Y. Chen, *J. Mater. Chem. A* **2020**, *8*, 21756.
16. T. X. Nguyen, J. Patra, J. K. Chang, J. M. Ting, *J. Mater. Chem. A* **2020**, *8*, 18963.
17. D. Wang, S. Jiang, C. Duan, J. Mao, Y. Dong, K. Dong, Z. Wang, S. Luo, Y. Liu, X. Qi, *J. Alloys Compd.* **2020**, *844*, 156158.
18. C. Duan, K. Tian, X. Li, D. Wang, H. Sun, R. Zheng, Z. Wang, Y. Liu, *Ceram. Int*. **2021**, *47*, 32025.
19. H. Z. Xiang, H. X. Xie, X. X. Chen, H. Zhang, A. Mao, C. H. Zheng, *J Mater Sci* **2021**, *56*, 8127.
20. M. Kheradmandfard, H. Minouei, N. Tsvetkov, A. K. Vayghan, S. F. K. Bozorg, G. Kim, S. I. Hong, D. E. Kim, *Mat. Chem. Phys*. **2021**, *262*, 124265.
21. J. Wei, K. Rong, X. Li, Y. Wang, Z. A. Qiao, Y. Fang, S. Dong, *Nano Res*. **2021**, https://doi.org/10.1007/s12274-021-3860-7.
22. C. Y. Huang, C. W. Huang, M. C. Wu, J. Patra, T. X. Nguyen, M. T. Chang, O. Clemens, J. M. Ting, J. Li, J. K. Chang, *Chem. Eng. J*. **2021**, *420*, 129838.
23. J. Zhao, X. Yang, Y. Huang, F. Du, Y. Zeng, *ACS Appl. Mater. Interfaces* **2021**, *13*, 58674.
24. B. Xiao, G. Wu, T. Wang, Z. Wei, Y. Sui, B. Shen, J. Qi, F. Wei, Q. Meng, Y. Ren, X. Xue, J. Zheng, J. Mao, K. Dai, *Ceram. Int*. **2021**, *47*, 33972.
25. H. Chen, N. Qiu, B. Wu, Z. Yang, S. Sun, Y. Wang, *RSC Adv*. **2020**, *10*, 9736.
26. T. X. Nguyen, C. C. Tsai, J. Patra, O. Clemens, J. K. Chang, J. M. Ting, *Chem. Eng. J*. **2020**, *430*, 132658.

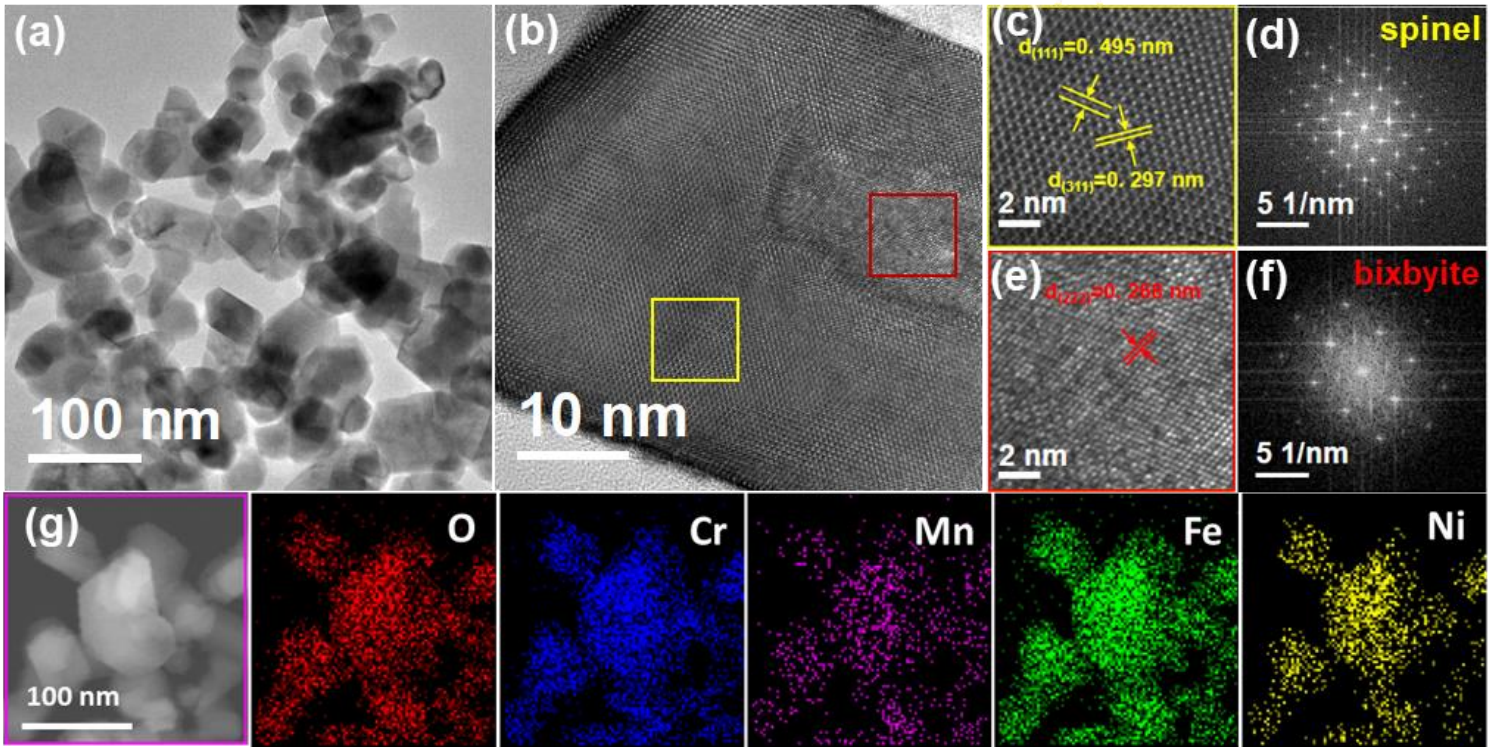

Figure S1. (a) TEM image, (b) high-resolution lattice image, (c) enlarge yellow region with the corresponding FFT pattern (d), (e) enlarge red region with the corresponding FFT pattern (f), and (g) HAADF image/EDS mapping data of as-synthesized 4M sample.

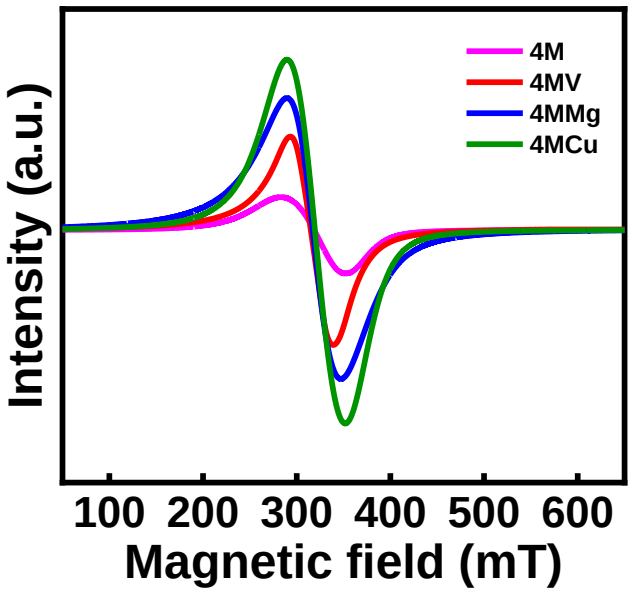

Figure S2. Electron paramagnetic resonance data of 4M, 4MV, 4MMg, and 4MCu samples.

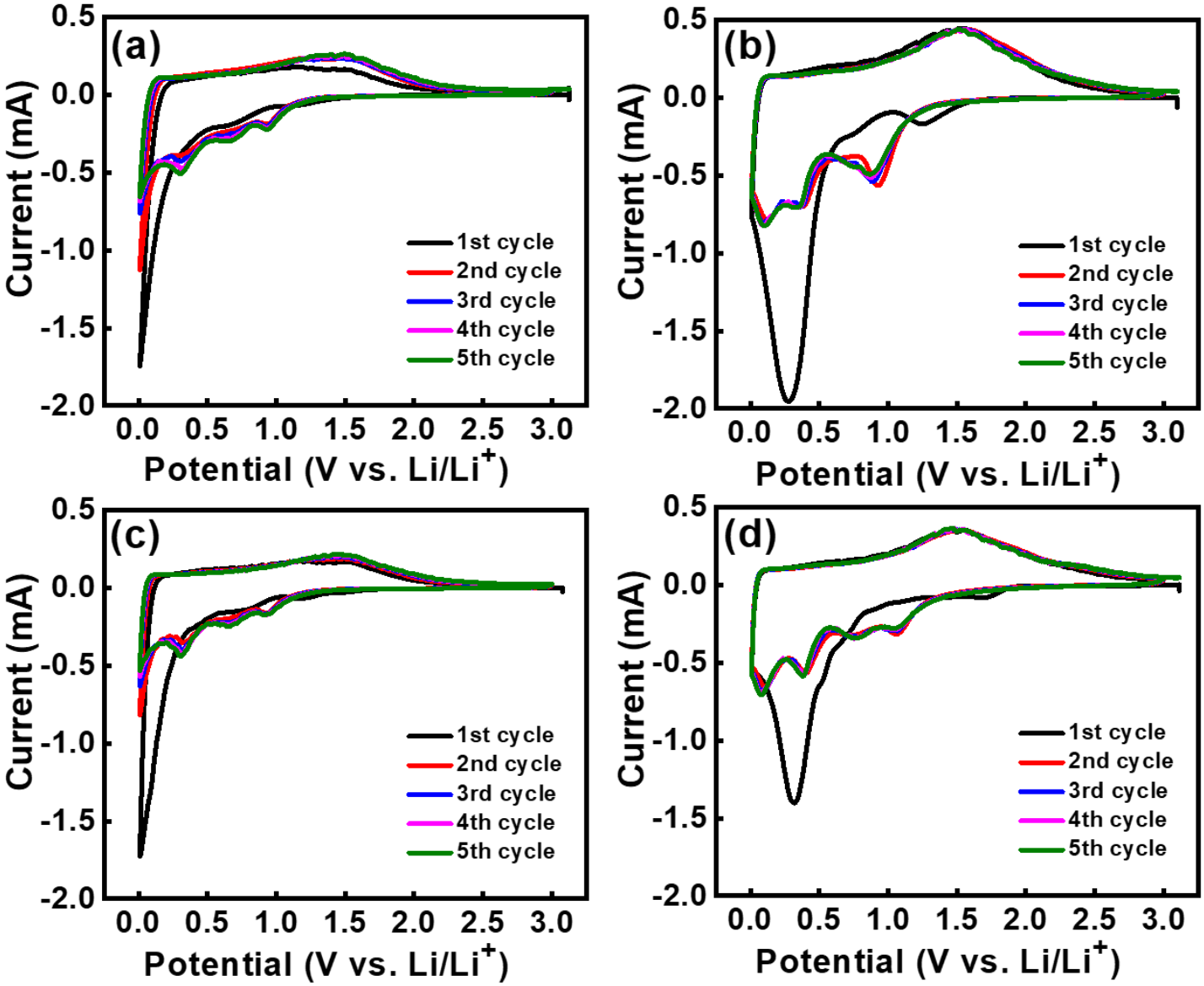

Figure S3. CV curves of (a) 4M, (b) 4MV, (c) 4MMg, and (d) 4MCu electrodes recorded at potential sweep rate of 0.1 mV s^{-1}.

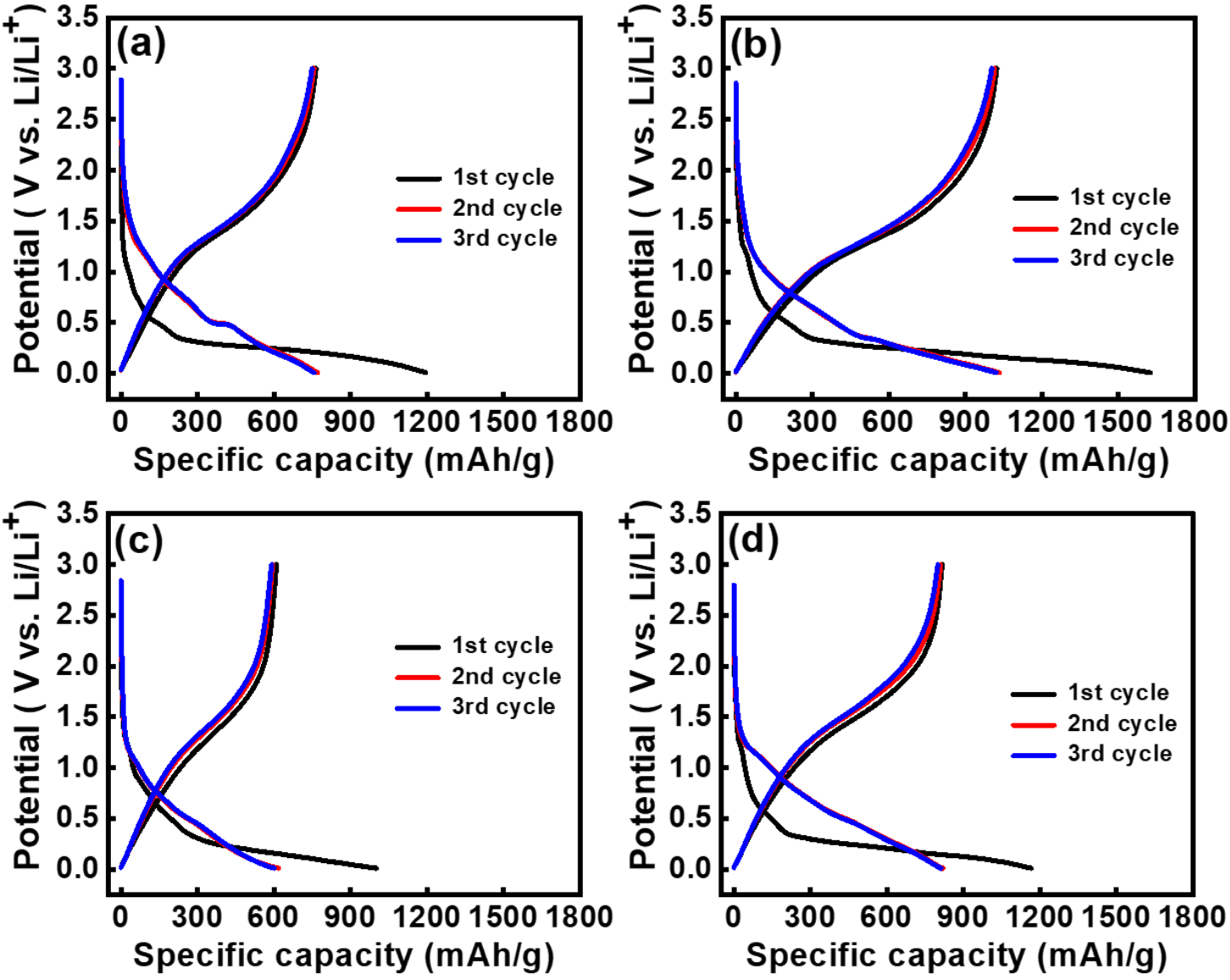

Figure S4. Initial three charge-discharge curves of (a) 4M, (b) 4MV, (c) 4MMg, and (d) 4MCu electrodes measured at 50 mA g^{-1}.

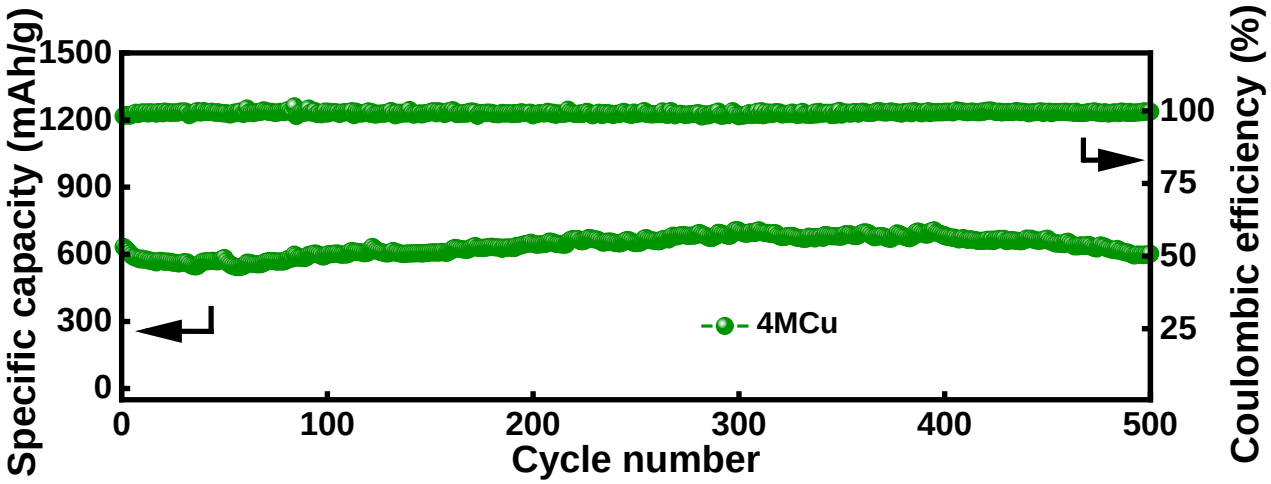

Figure S5. Cycling stability of 4MCu electrode measured at 500 mA g^{-1} for 500 cycles.

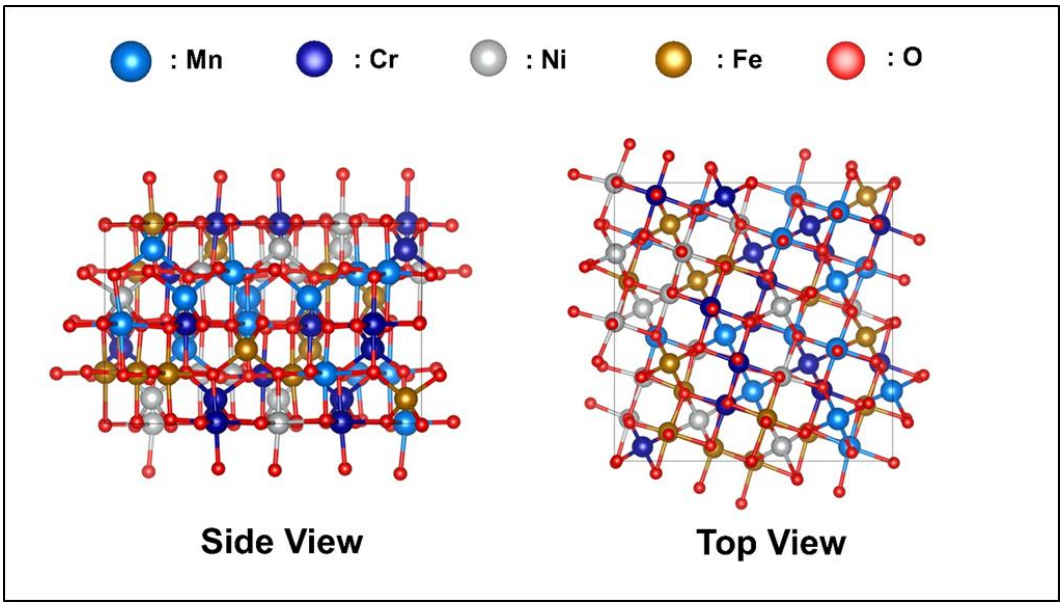

Figure S6. Optimized structure of 4M spinel oxide containing 140 atoms with formation energy of 4.44 eV.

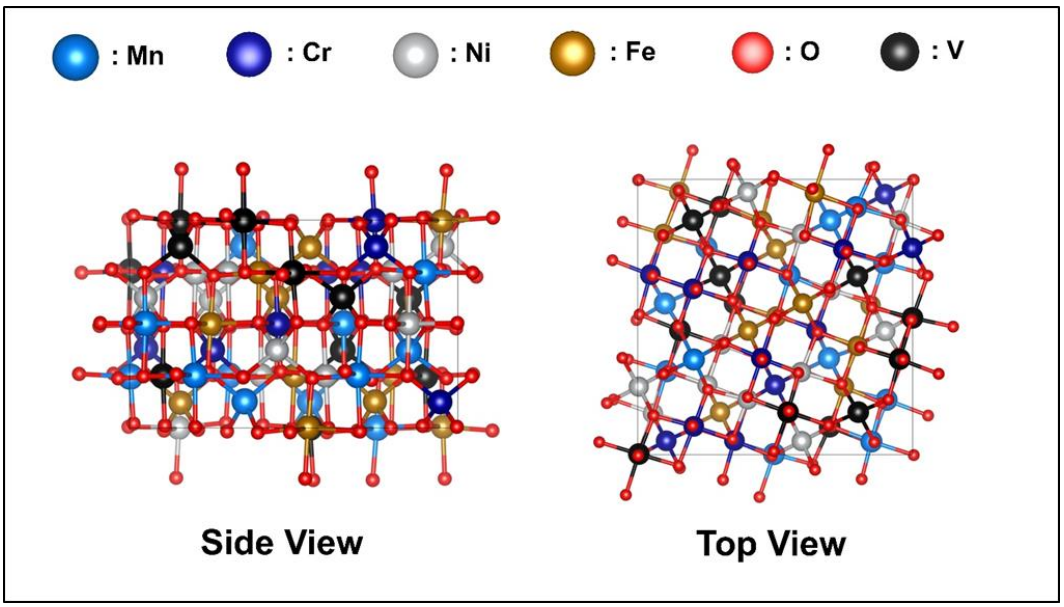

Figure S7. Optimized structure of 4MV spinel oxide containing 140 atoms with formation energy of 4.65 eV.

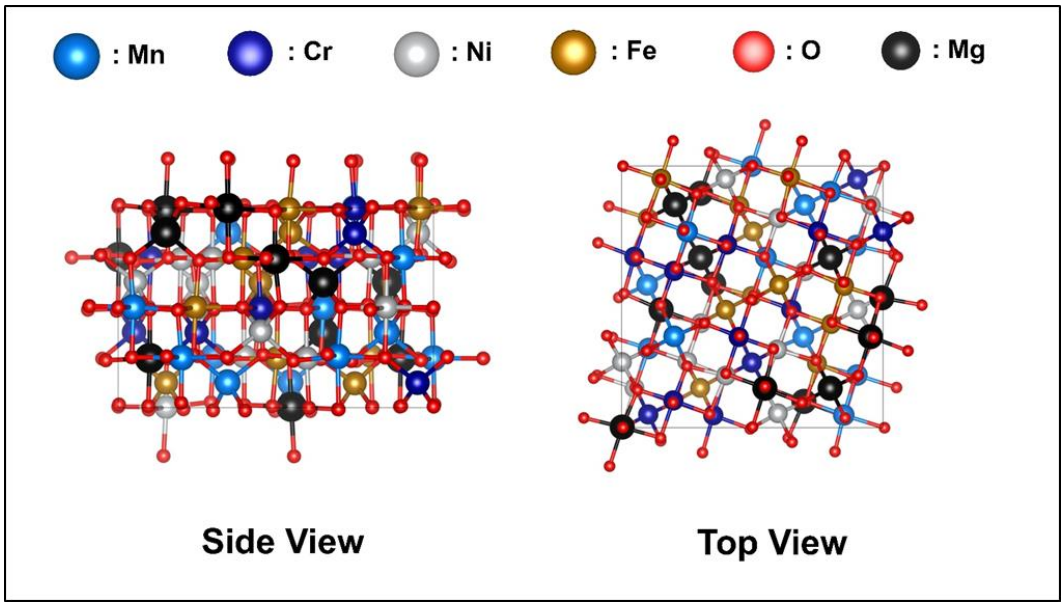

Figure S8. Optimized structure of 4MMg spinel oxide containing 140 atoms with formation energy of 6.91 eV.

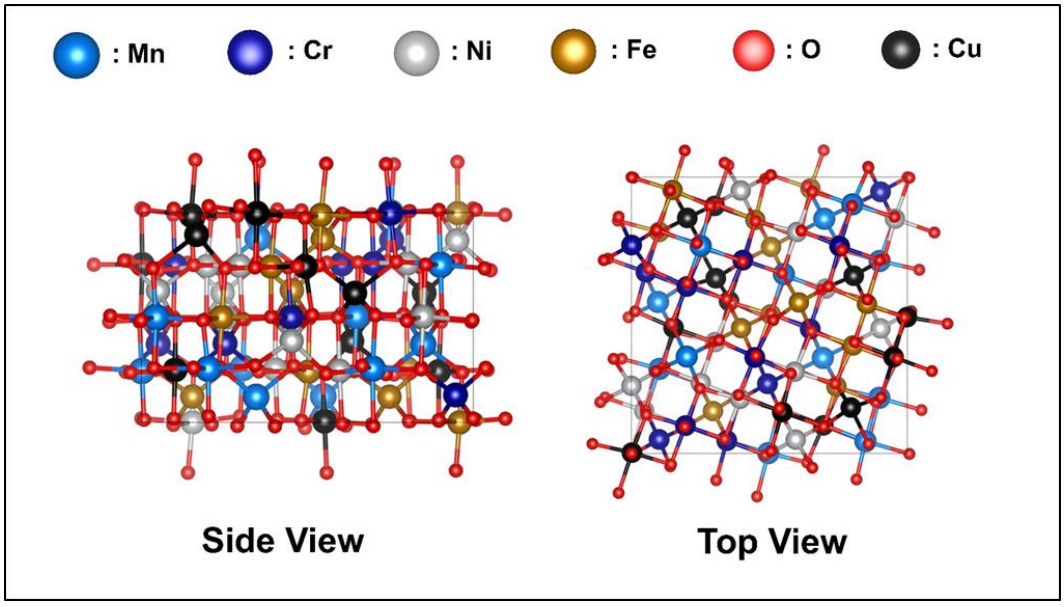

Figure S9. Optimized structure of 4MCu spinel oxide containing 140 atoms with formation energy of 3.14 eV.

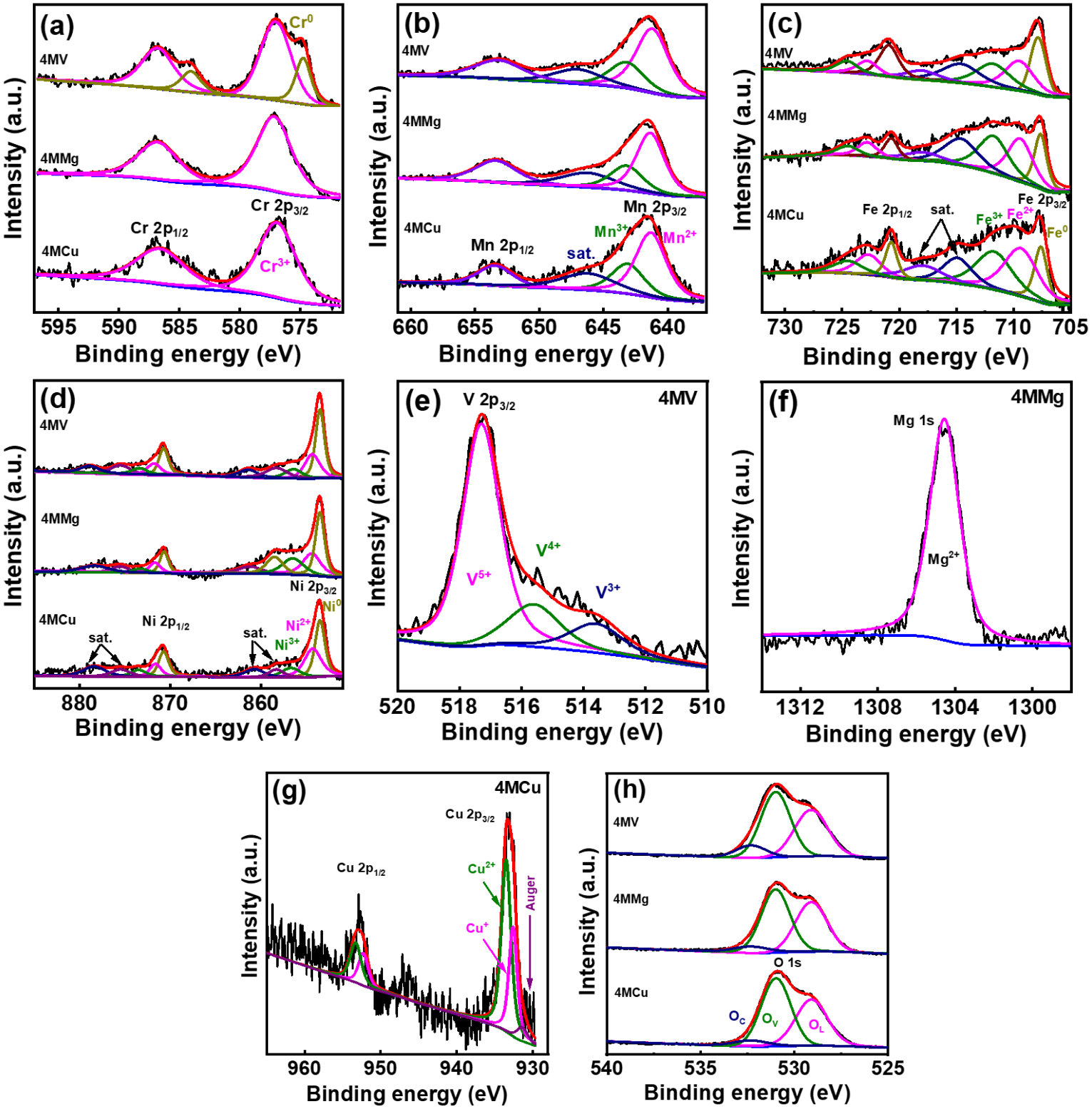

Figure S10. High-resolution XPS (a) Cr 2p, (b) Mn 2p, (c) Fe 2p, (d) Ni 2p, (e) V $2p_{3/2}$, (f) Mg 1s, (g) Cu 2p, and (h) O 1s spectra of various samples after cycling.